SEDIMENTOLOGY the journal of the International Association of Sedimentologists

Sedimentology (2022) **69**, 1861–1890 doi: 10.1111/sed.12975

Tidal dynamics in palaeo-seas in response to changes in physiography, tidal forcing and bed shear stress

VALENTIN ZUCHUAT*,† , ELISABETH STEEL‡ , RYAN P. MULLIGAN§ , DANIEL S. COLLINS¶ and J. A. MATTIAS GREEN**

**Geological Institute, RWTH-Aachen University, Wüllnerstrasse 2, Aachen, 52062, Germany (E-mail: valentin.zuchuat@emr.rwth-aachen.de)*

†Department of Geosciences, University of Oslo, Sem Sælands Vei 1, Oslo, 0371, Norway

‡Department of Geological Sciences and Geological Engineering, Queen's University, 36 Union Street, Kingston, ON, K7L 3N6, Canada

§Department of Civil Engineering, Ellis Hall, Queen's University, Kingston, ON, K7L 3N6, Canada

¶Shell International Limited, Shell Centre, London, SE1 7NA, UK

***School of Ocean Sciences, Bangor University, Menai Bridge, LL59 5AB, UK*

Associate Editor – Massimiliano Ghinassi

ABSTRACT

Simulating hydrodynamic conditions in palaeo-ocean basins is needed to better understand the effects of tidal forcing on the sedimentary record. When combined with sedimentary analyses, hydrodynamic modelling can help inform complex temporal and spatial variability in the sediment distribution of tide-dominated palaeo-ocean basins. Herein, palaeotidal modelling of the epicontinental Upper Jurassic (160 Ma, lower Oxfordian) Sundance and Curtis seas of North America reveals possible regional-scale variations in tidal dynamics in response to changes in ocean tidal forcing, physiographic configuration and bottom drag coefficient. A numerical model forced with an M2 tidal constituent at the open boundary shows that the magnitude and location of tidal amplification, and the variability in current velocity and bed shear stress in the basin, were controlled by palaeophysiography. Numerical results obtained using a depth of 600 m at the ocean boundary of the system enable the prediction of major facies trends observed in the lower Curtis Formation. The simulation results also highlight that certain palaeophysiographic configurations can either permit or prevent tidal resonance, leading to an overall amplification or dampening of tides across the basin. Furthermore, some palaeophysiographic configurations generated additional tidal harmonics in specific parts of the basins. Consequently, similar sedimentary successions can emerge from a variety of relative sea-level scenarios, and a variety of sedimentary successions may be deposited in different parts of the basin in any given relative sea-level scenario. These results suggest that the interpretation of sedimentary successions deposited in strongly tide-influenced basins should consider changes in tidal dynamics in response to changing sea level and basin physiography.

Keywords Curtis Formation, non-uniqueness, numerical modelling, palaeoceanography, relative sea-level change, sequence stratigraphy, tidal deposits, Upper Jurassic.

INTRODUCTION

Tides have been observed, measured and predicted for centuries (if not millennia) by seafarers across the world (Cartwright, 2001) despite a very limited understanding of the astronomical mechanics behind them. It is now well-understood that variations in the force of gravity caused by periodic motions of the Moon, Earth and Sun generate the components of the observed tidal water level elevations. Today, 630 tidal harmonic constituents (Simon & Page, 2017) can be used to mathematically solve, model and predict the propagation of modern tides, although far fewer constituents are normally used for predictions at specific locations (Fang *et al.*, 1999; Hess, 2003; Pelling *et al.*, 2013; Ashall *et al.*, 2016; Kresning *et al.*, 2019; Mulligan *et al.*, 2019a). Of these, the semi-diurnal M2-lunar constituent is commonly the most important, which, when combined with the strongest solar constituent S2, causes neap–spring tidal cycles (Parker, 2007).

There is no shortage of tidal evidence in the ancient rock record (Eriksson, 1977; Kvale & Archer, 1991; Räsänen *et al.*, 1995; Kvale, 2006; Raaf & Boersma, 2007; James *et al.*, 2010; Davis *et al.*, 2012; Longhitano *et al.*, 2012; Gugliotta *et al.*, 2015; Rossi *et al.*, 2016; Fritzen *et al.*, 2019; Collins *et al.*, 2020; Phillips *et al.*, 2020), although some of the concepts developed from the study of ancient tidally-influenced sedimentary strata can be inconsistent with phenomena recognized in modern tidal environments (see discussion in Gugliotta & Saito, 2019; Cosma *et al.*, 2020; Finotello *et al.*, 2020). Numerical modelling of ancient basins (Wells *et al.*, 2010; Hill *et al.*, 2011; Mitchell *et al.*, 2011; Collins *et al.*, 2018; Dean *et al.*, 2019; Green *et al.*, 2020; Collins *et al.*, 2021; Daher *et al.*, 2021) can help to test hypotheses formulated from the study of the rock record, reduce discrepancies between interpreted ancient and modern tides and tidal deposits, and improve the calibration of ancient tidal signals to astronomical parameters. Complementarily, the rock record can help to constrain model inputs and interpret results (Ward *et al.*, 2015; Dean *et al.*, 2019; Byrne *et al.*, 2020; Green *et al.*, 2020; Haigh *et al.*, 2020; Collins *et al.*, 2021; Daher *et al.*, 2021) and exclude anomalous 'numerically-viable' simulations (Ward *et al.*, 2020). The integration of field data and numerical modelling also helps to test, quantify and visualize the spatio-temporal changes in tidal processes resulting from changes in basin configuration (Collins *et al.*, 2021). For instance, in depositional basins, the sedimentary record can be interpreted and numerical models can be used to confirm or enhance knowledge of these systems (Mallinson *et al.*, 2018; Mulligan *et al.*, 2019b). This increased knowledge of past basins will improve understanding of how tidal processes will evolve in response to today's sea-level rise, including assisting coastal areas in their planning by demonstrating how and where the tidal regime will significantly change (Hayden *et al.*, 2020).

The primary aim of this paper is to study and quantify the impact of changing palaeophysiography, initial open-ocean tidal forcing and bed shear stress on the behaviour of tides across an epicontinental sea. This, in return, will help to refine the interpretation of the sedimentary record when implemented into basin models. Through a series of numerical modelling experiments, this study highlights the consequences that variations in these initial conditions can have on interpreting the history and sequence stratigraphy of tidally-influenced sedimentary successions. Specific objectives are to: (i) simulate the propagation of tides in the Jurassic Sundance and Curtis seas in present day Utah, USA (Fig. 1) using a range of potential palaeophysiographies, initial open-ocean tidal forcing inputs, and bed shear stress values to assess their impact on tidal processes; (ii) compare sediment distribution proxies derived from simulated flow speed and bed shear stress values

Fig. 1. (A) Palaeogeographical map of the world during the Oxfordian (Lower Jurassic), 160 Ma. The red outline indicates the area of interest. (B) Zoomed-in palaeogeographical map of the Sundance and Curtis seas. The Entrada Desert on the coastal plain of the Curtis Sea (CS) is a potential source of sediment for the southernmost part of the Curtis Sea. This palaeogeographical reconstruction corresponds to the time when the lower Curtis was being deposited [Zuchuat *et al.*, 2018; maps (A) and (B) from Deep Time Maps™, ©2016 Colorado Plateau Geosystems Inc.]. (C) Palaeophysiography of the Sundance and Curtis seas area, with a 600 m maximum depth at the mouth of the corridor, with location of the control points (D) used in this paper. The red square indicates the area surveyed by Zuchuat *et al.* in their 2018, 2019a,b papers.

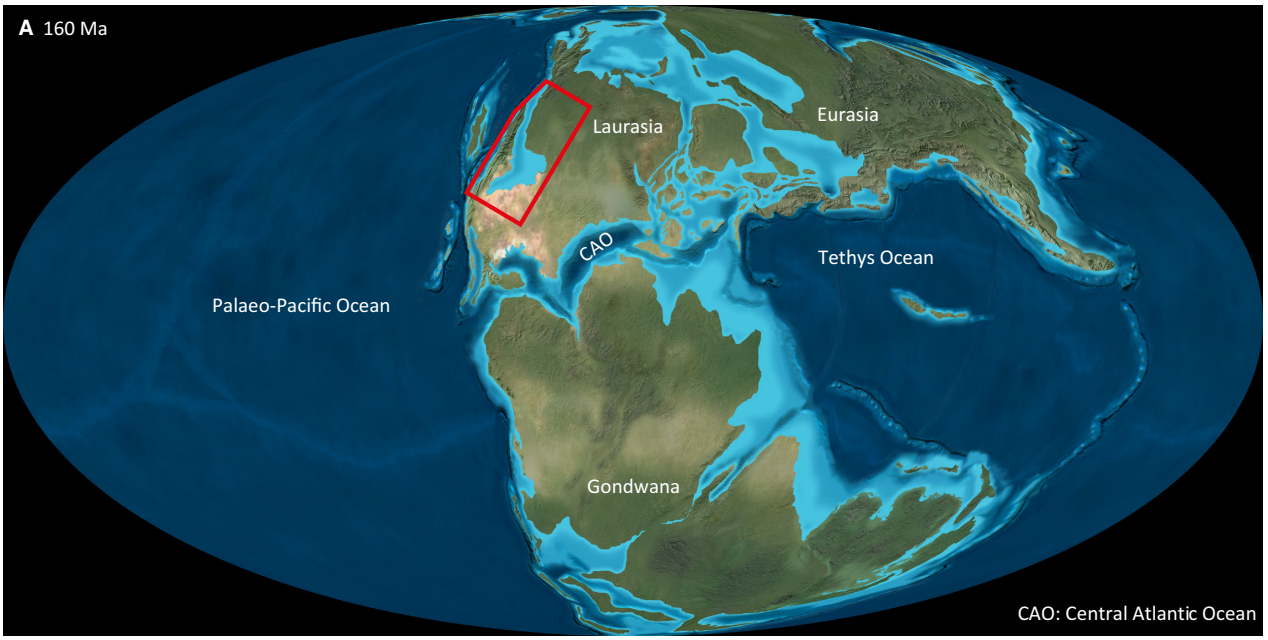

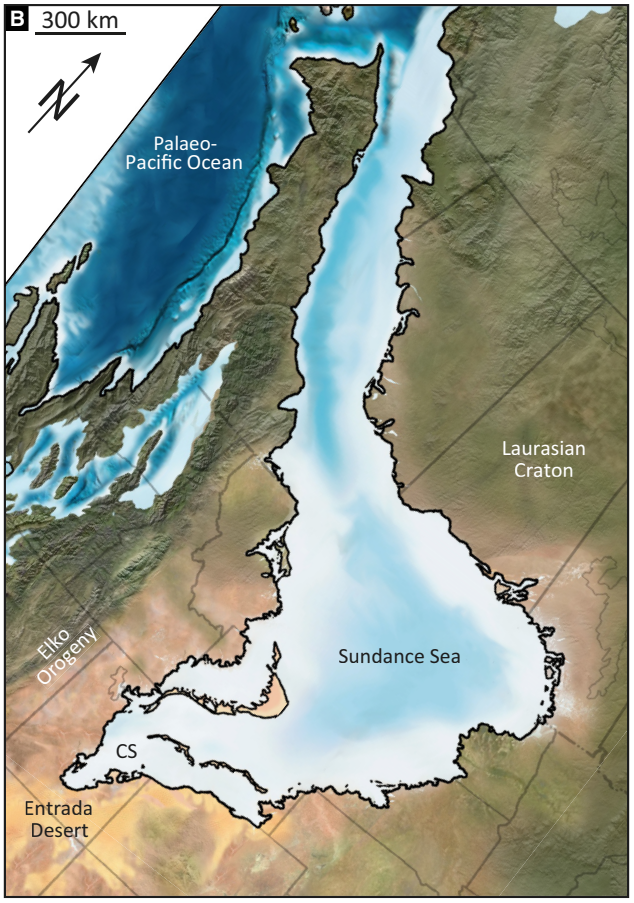

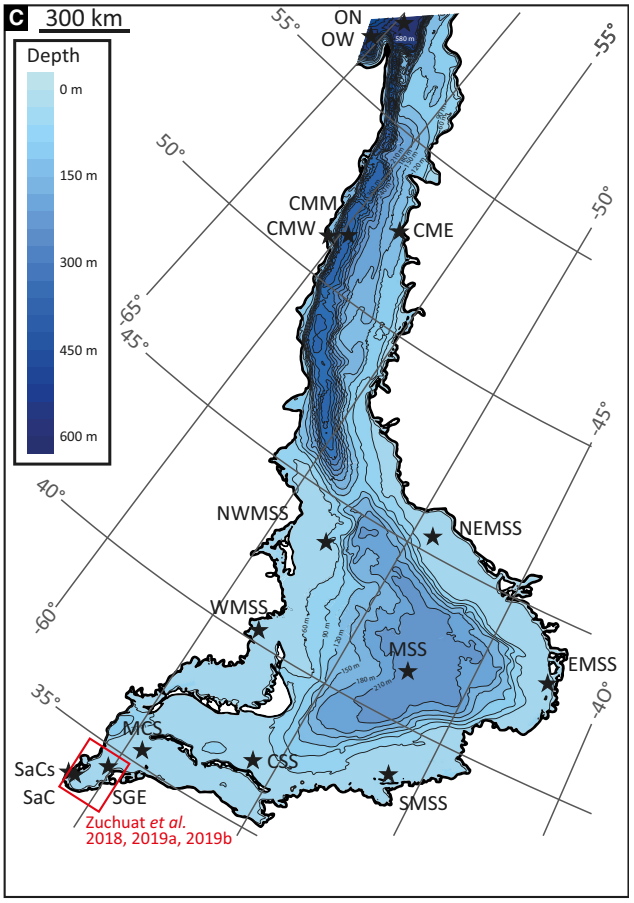

Key locations D

Ocean North (ON)	NW-Margin Sundance Sea (NWMSS)	South Margin Sundance Sea (SMSS)
Ocean West (OW)	NE-Margin Sundance Sea (NEMSS)	Curtis-Sundance Sea (CSS)
Corridor Middle West (CMW)	West-Margin Sundance Sea (WMSS)	Middle Curtis Sea (MCS)
Corridor Middle Middle (CMM)	Middle Sundance Sea (MSS)	Stove Gulch East (SGE)
Corridor Middle East (CME)	East-Margin Sundance Sea (EMSS)	Sid And Charley (SaC)
		Sid And Charley Shallow (SaCs)

Zuchuat *et al.* (2018, 2019a, 2019b)

(Ward *et al.*, 2015, 2020) to deposits of the Upper Jurassic Curtis Formation of the innermost Curtis Sea, using the rocks to inform the models (in a similar fashion as Byrne *et al.*, 2020; Green *et al.*, 2020; and Daher *et al.*, 2021); and (iii) analyse the implications of these simulation results on basin history and sequence stratigraphy of similar systems.

GEOLOGICAL CONTEXT

During the Middle and Late Jurassic, the 2500 km long Sundance Sea (Fig. 1), also known as the proto-Western Interior Seaway (Blakey, 2014), developed in a retroarc foreland basin (Brenner & Peterson, 1994; Bjerrum & Dorsey, 1995). This seaway spanned between present day Wyoming and British Columbia, where it was connected to the Palaeo-Pacific Ocean (Imlay, 1952, 1980; Blakey, 2014). During the Callovian and Oxfordian, the Sundance Sea periodically extended an additional *ca* 1500 km south-westward (Imlay, 1952; Pipiringos & O'Sullivan, 1978; Peterson, 1994; Imlay, 1980; Kreisa & Moila, 1986; Caputo & Pryor, 1991; Anderson & Lucas, 1994; Brenner & Peterson, 1994; Peterson, 1994; Wilcox & Currie, 2008; Hintze & Kowallis, 2009; Sprinkel *et al.*, 2011; Thorman, 2011; Doelling *et al.*, 2013; Danise & Holland, 2017, 2018; Zuchuat *et al.*, 2018, 2019a,b; Danise *et al.*, 2020), flooding the SSW–NNE-oriented retroarc foreland basin known as the Utah–Idaho Trough (Bjerrum & Dorsey, 1995), which developed at the foot of the Elko Orogeny (Thorman, 2011; Anderson, 2015). These repeated south-westward incursions (Zuchuat *et al.*, 2019a) from the Sundance Sea led to the deposition of two shallow-marine sedimentary units that crop out today in east-central Utah: The Callovian Carmel Formation and the Oxfordian Curtis Formation. The Carmel Formation (Gilluly & Reeside, 1928) primarily consists of limestone and evaporites, and was deposited as the Carmel Sea transgressed over the arid continental Temple Cap Formation (Doelling *et al.*, 2013). The arid coastal plain deposits of the Entrada Sandstone were deposited during the subsequent regression (Crabaugh & Kocurek, 1993; Peterson, 1994; Carr-Crabaugh & Kocurek, 1998). A second, pulsed marine transgression occurred during the Oxfordian (Wilcox & Currie, 2008; Zuchuat *et al.*, 2019a), shortly after 161 Ma (Dossett, 2014), and led to the deposition of the siliciclastic-rich Curtis Formation (Fig. 2; Gilluly & Reeside, 1928). The Curtis Formation is conformably overlain by arid mudflats of the Summerville Formation (Gilluly & Reeside, 1928), which developed as the Curtis Sea regressed towards the north-east (Caputo & Pryor, 1991; Wilcox & Currie, 2008; Zuchuat *et al.*, 2019a).

Both the Carmel Formation and the Curtis Formation were strongly influenced by tidal currents at the time of their deposition (Fig. 3; Kreisa & Moila, 1986; Caputo & Pryor, 1991; Wilcox & Currie, 2008; Doelling *et al.*, 2013; Zuchuat *et al.*, 2018, 2019a,b). Evidence of strong tidal currents include: common heterolithic lithologies, inclined heterolithic strata, rhythmites, tidal bundles and flaser bedding (both of which are often combined with additional indications of periodic waxing and waning of the flow, i.e. thickening and thinning of the strata and foresets). There is also robust sedimentary and statistical evidence of recurrent flow reversals, comprising reactivation surfaces in compound dunes (some associated with subordinate counter-current ripples at their toes), bidirectionally-accreting bar-forms and herringbone cross-stratification (Zuchuat *et al.*, 2018). Indicators of wave activity are extremely scarce in the Curtis Formation, although it does not necessarily imply that these processes were completely inactive at the time of deposition (van Yperen *et al.*, 2020). Nevertheless, the lack of preservation of wave markers associated with the abundant tidal indicators suggests that tides were the more dominant process in the Curtis Sea. Additionally, the Curtis Sea was bounded by the arid Entrada continental plains, in which no perennial fluvial systems developed, therefore drastically limiting the possible influence of rivers on the deposition of the Curtis Formation (Kreisa & Moila, 1986; Caputo & Pryor, 1991; Wilcox & Currie, 2008; Doelling *et al.*, 2013; Zuchuat *et al.*, 2018, 2019a,b).

The correlative units of the Curtis–Summerville interval towards the Sundance Sea are the Stump Formation (Mansfield & Roundy, 1916; Pipiringos & O'Sullivan, 1978; Imlay, 1980; Patterson-Wittstrom, 1980; Wilcox & Currie, 2008; Jensen *et al.*, 2016; Kowallis *et al.*, 2018) and the Redwater Shale Member of the Sundance Formation (Imlay, 1947, 1980; Patterson-Wittstrom, 1980; Uhlir *et al.*, 1988). The mudstones of the Redwater Shale Member record deposition in the deeper part of the Sundance Sea (Imlay, 1980; Danise & Holland, 2018) and experienced limited tidal influence. In contrast, the heterolithic Stump Formation, which

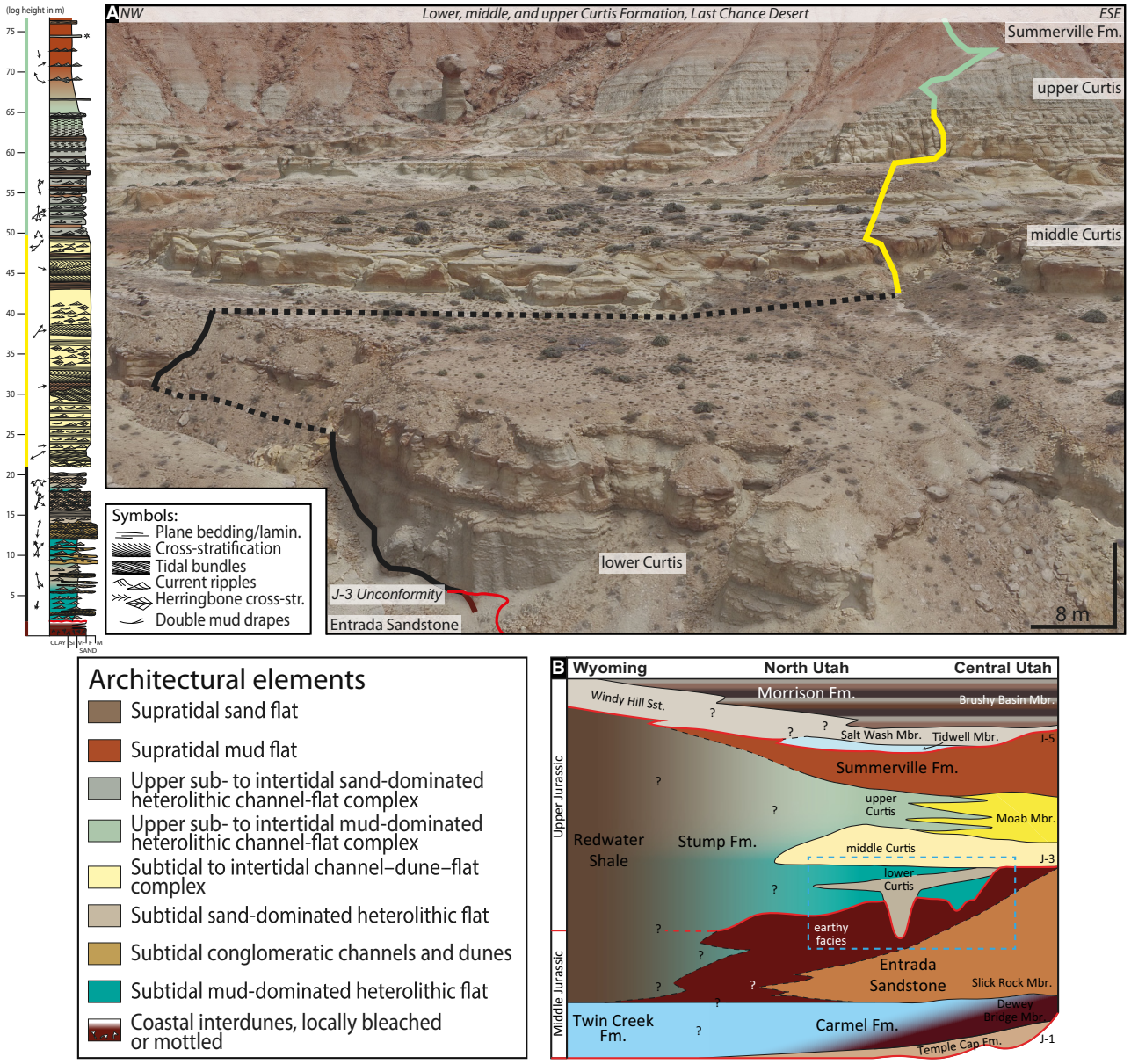

Fig. 2. (A) Photograph of the Curtis Formation accompanied by a sedimentary log detailing the stratigraphic architecture of the formation. The Curtis Formation is subdivided into three informal subunits: the thinly-bedded, heterolithic, lower Curtis (black trace); the well-sorted, cross-stratified and amalgamated, middle Curtis (yellow trace); and the fining-upward, tabular, upper Curtis (light green trace; Zuchuat *et al.*, 2018). This paper will focus on the development of the lower Curtis only. (B) Schematic panel displaying the part of the Middle and Upper Jurassic lithostratigraphy cropping out between Central Utah and Wyoming (after Doelling *et al.*, 2013; Danise & Holland, 2017; Zuchuat *et al.*, 2018; Danise *et al.*, 2020). Note that the J-3 and the J-5 unconformities are not regarded as unconformities *sensu stricto* anymore, but rather as a highly diachronous transgressive surface (Zuchuat *et al.*, 2019a) and the product of a prograding braided fluvio-deltaic system unimpacted by relative sea-level fall (Danise *et al.*, 2020), respectively.

mostly consists of glauconitic sandstone, muddy siltstone and oolitic limestone (Pipiringos & O'Sullivan, 1978; Imlay, 1980; Patterson-Wittstrom, 1980; Jensen *et al.*, 2016; Kowallis *et al.*, 2018), was influenced by tidal processes at the time of deposition (Wilcox & Currie, 2008). North of the central Sundance Sea and up to the connection with the open ocean, the climate was more temperate than the arid climate prevailing around the Curtis Sea (Sellwood

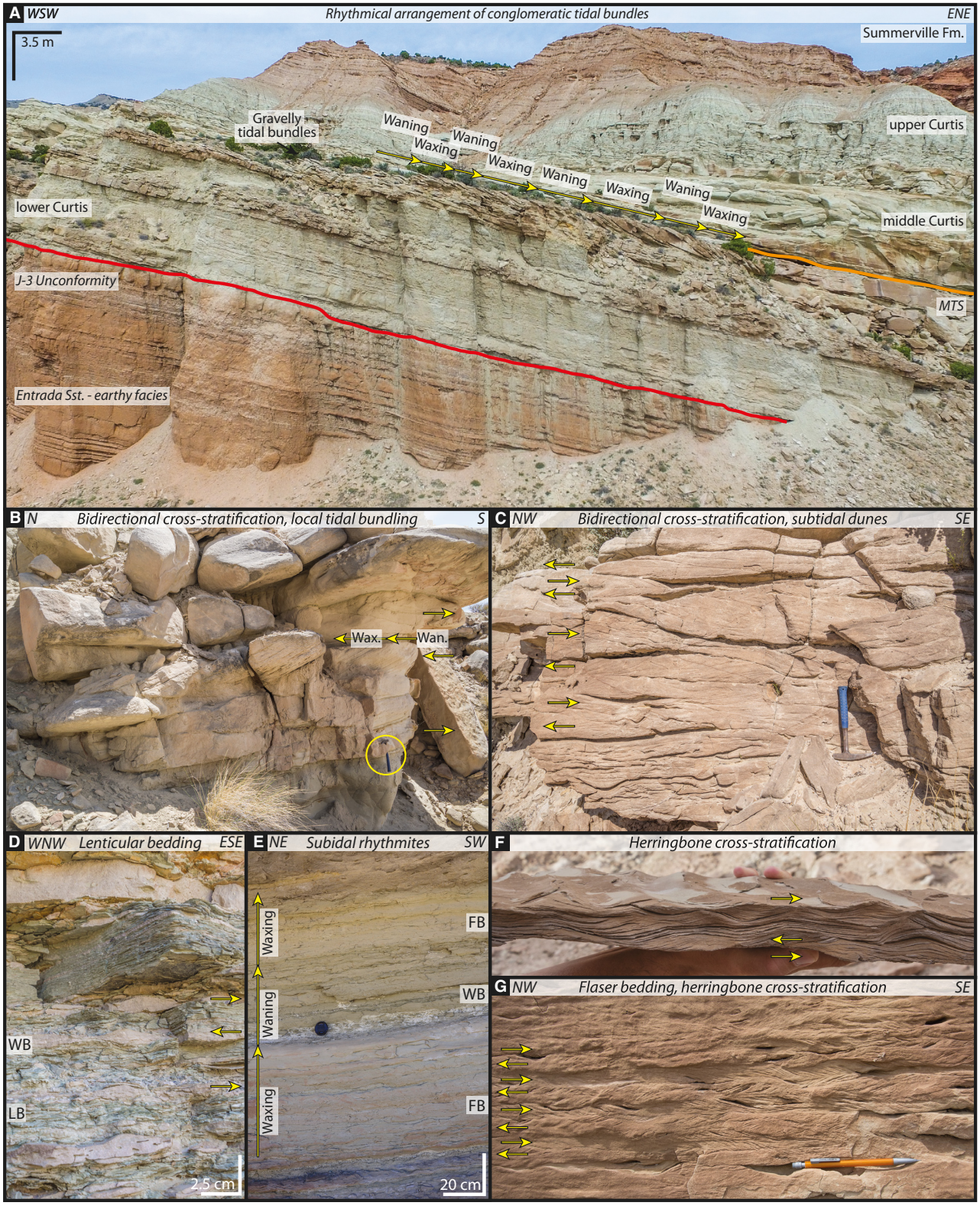

& Valdes, 2006; Uhl *et al.*, 2012). As the Oxfordian regression of the Curtis Sea persisted and the climate became more humid (Demko *et al.*, 2004; Boucot *et al.*, 2013; Danise & Holland, 2017), the shoreline developed as a tide-dominated deltaic system (Holland & Wright,

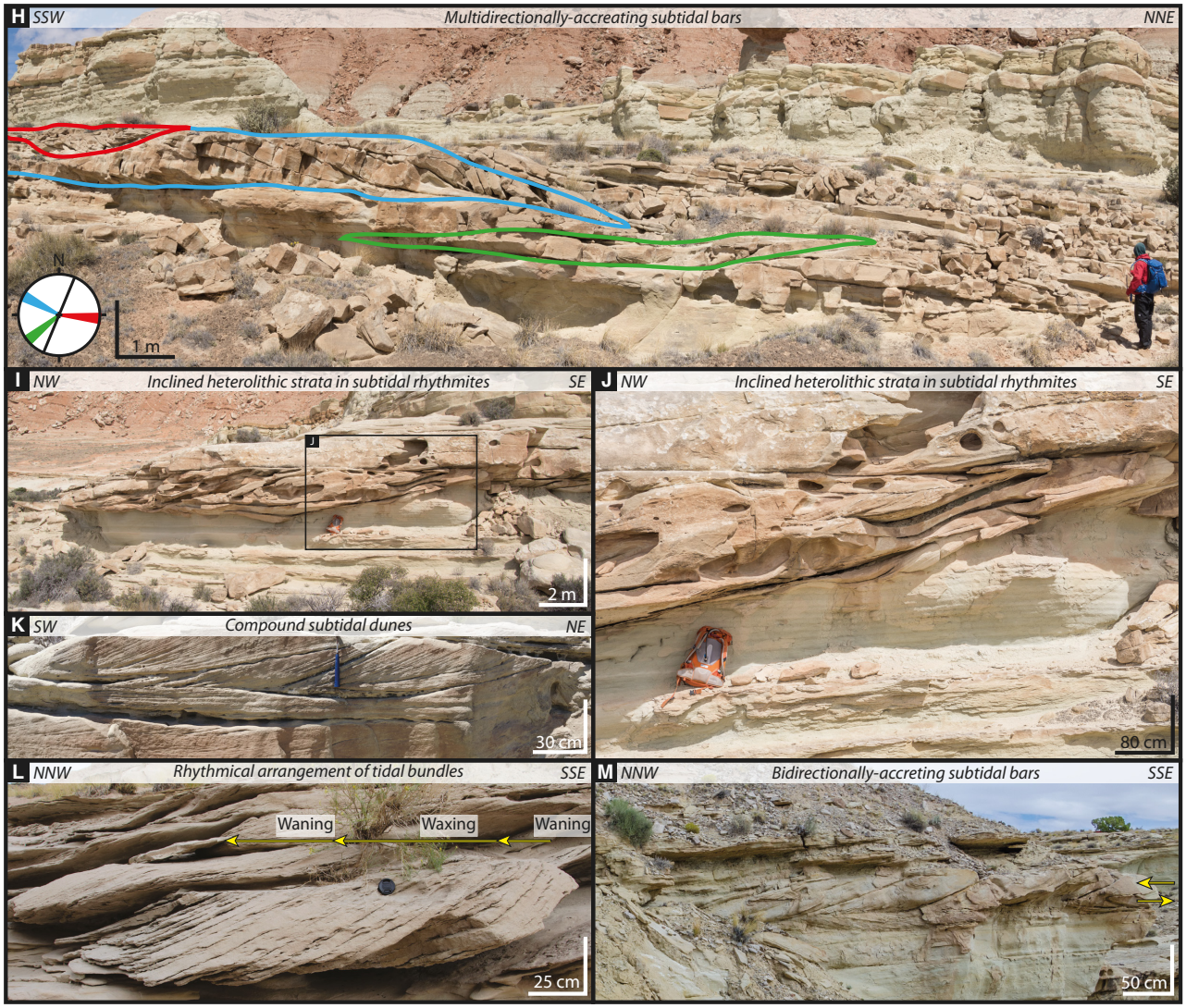

Fig. 3. Example of sedimentary bedforms diagnostic of tidal currents. (A) Rhythmical development of conglomeratic tidal bundles following phases of waxing and waning of tidal currents. (B) Bidirectional cross-stratification in stacked, three-dimensional (3D) subtidal dunes, with local waxing–waning architecture. Hammer for scale (yellow circle, *ca* 32 cm long). (C) Bidirectional cross-stratification in 3D subtidal dunes. Hammer for scale. (D) Heterolithic strata, deposited as lenticular (LB) and wavy bedding (WB), with bidirectional, ripple cross-stratified sandstone lenses. (E) Subtidal rhythmites, testifying to phases of waxing and waning tidal currents. (F) Bidirectional ripple cross-stratified sandstone bed (herringbone cross-stratification). Hand for scale. (G) Flaser bedded sandstone, with bidirectional ripple cross-stratification. Pencil for scale (*ca* 15 cm long). (H) Colour-coded, multidirectionally-accreting subtidal bars. The black line on the rose diagram corresponds to the SSW–NNE orientation of the photograph. Geologist for scale (1.80 m). (I) and (J) Inclined heterolithic strata, product of the lateral migration of the meander of subtidal-channel, incising into subtidal rhythmites. (Backpack for scale, height *ca* 75 cm). (K) Compound, 3D subtidal dune with multiple reactivation surfaces. (L) Rhythmical development of sigmoidal tidal bundles following phases of waxing and waning of tidal currents. (M) Bidirectional migration of subtidal bars.

2020). These sandstone-dominated strata, which belong to the Windy Hill Member of the Morrison Formation (Pipiringos, 1979), indicate that tidal currents lingered despite a shrinking sea (Uhlir *et al.*, 1988; Danise & Holland, 2018; Holland & Wright, 2020). As a result, fluvial processes might have impacted the coastal dynamics locally, but the lack of geological record prevents any interpretation of where and how strong these fluvial processes were.

The lack of high-resolution biostratigraphy and absolute dating of the Curtis–Summerville interval makes precise regional correlation between units in the Curtis and Sundance seas challenging. Models in this study are therefore based on localities that can be well-constrained (for example, innermost Curtis Sea).

METHODS

Numerical modelling

The geological record from the innermost Curtis Sea is relatively well-constrained (Gilluly & Reeside, 1928; Pipiringos & O'Sullivan, 1978; Kreisa & Moila, 1986; Caputo & Pryor, 1991; Wilcox & Currie, 2008; Doelling *et al.*, 2013; Danise & Holland, 2017, 2018; Zuchuat *et al.*, 2018, 2019a,b; Danise *et al.*, 2020) and was used to inform and interpret series of numerical modelling experiments in Delft3D. The methods employed in this study followed common practice for hydrodynamic modelling in present-day tidal basins (Hu *et al.*, 2009; Elias *et al.*, 2012; Brown *et al.*, 2014; Mulligan *et al.*, 2015; Mulligan *et al.*, 2019b); however, the lack of observations of water levels and currents necessitate the use of geological interpretations of palaeoenvironmental conditions. The modelling of tides in the Upper Jurassic Sundance and Curtis seas used the Oxfordian palaeogeographical map (Fig. 1) from Deep Time Maps™ (Colorado Plateau Geosystems Inc. Maps), which was palaeogeoreferenced using GPlates (Müller *et al.*, 2018) and projected on a Lambert Conformal Conic projection. Various palaeophysiographies were generated by converting the maps to a physiographic raster (Python code; Appendix A) and importing them into Deltares open-source Delft3D numerical modelling software. Delft3D is a three-dimensional hydrodynamic simulation suite used for solving hydrostatic and non-hydrostatic equations (see Delft3D user manual for details), and it has been used to model a variety of coastal systems, including river deltas, beaches, estuaries, lagoons and barrier islands–inlet systems (Hu *et al.*, 2009; Elias *et al.*, 2012; Brown *et al.*, 2014; Mulligan *et al.*, 2015; Mulligan *et al.*, 2019b). Due to the unknown true water depths and the need to investigate different realistic palaeophysiographies (Byrne *et al.*, 2020), a series of different depth grids were generated using the colour-gradient in the original palaeogeographical map. The shoreline (i.e. lightest colour on the map) is a finite boundary and was assigned a constant depth of 0 m, and the mouth of the system (the darkest map colour) was assigned depths of 300 m, 460 m, 555 m, 600 m, 645 m, 860 m, 1000 m, 1200 m and 1400 m to generate nine different depth scenarios (note that the name of each simulation used in this manuscript refers to these maximum depth values). Each depth scenario provided a different basin gradient from the mouth of the system to the inland shoreline, i.e. the shallower the depth at the mouth of the system, the shallower the basin gradient was.

The grid used to run the simulations was fixed and structured, and comprised 100,496 cells, which were approximately 3.4×3.4 km at the northern ocean boundary and 3.6×5.7 km in the southernmost part of the study area. The ocean boundary was an open boundary, allowing tidal flows to enter and exit the system. Shoreline boundaries were fitted to the coastline, and the relatively coarse resolution of the grid did not allow for detailed smaller-scale processes such the wetting and drying cycles of intertidal areas or flooding of the land surface to be accurately resolved; however, the details of these processes are of lesser importance to the regional scale in this study.

Because it was not possible to know the exact oscillation of the water level or the specific combination of tidal constituents that affected the studied system, the idealized tides were simulated in the basin using the dominant semi-diurnal M2 tidal constituent with the same period as today (i.e. 12.42 hr; Darwin, 1898; Pugh & Woodworth, 2014). Doing so allowed for unverifiable assumptions to be kept to a minimum, in line with previous modelling studies (e.g. Wells *et al.*, 2005a,b). The idealized approach of the M2 tidal boundary condition therefore enables interpretation of the complex tidal conditions that were generated within the sea. Other parameters such as the gravitational acceleration ($g = 9.81$ m/s^2) and fluid density ($\rho = 1025$ kg/m^3) were held constant. Even though neap–spring cycles are recognized in the Curtis Formation (Zuchuat *et al.*, 2018, 2019a), the modelling results did not resolve spring–neap oscillations, which would have required simulation of additional tidal constituents.

The simulations were run for 44 days using a one-minute time step (Fig. 4), which allowed the tides to reach steady-state. The exception was the simulation that used the 1430 m depth scenario, which was run for 134 days to allow the tides to reach equilibrium. This delay in

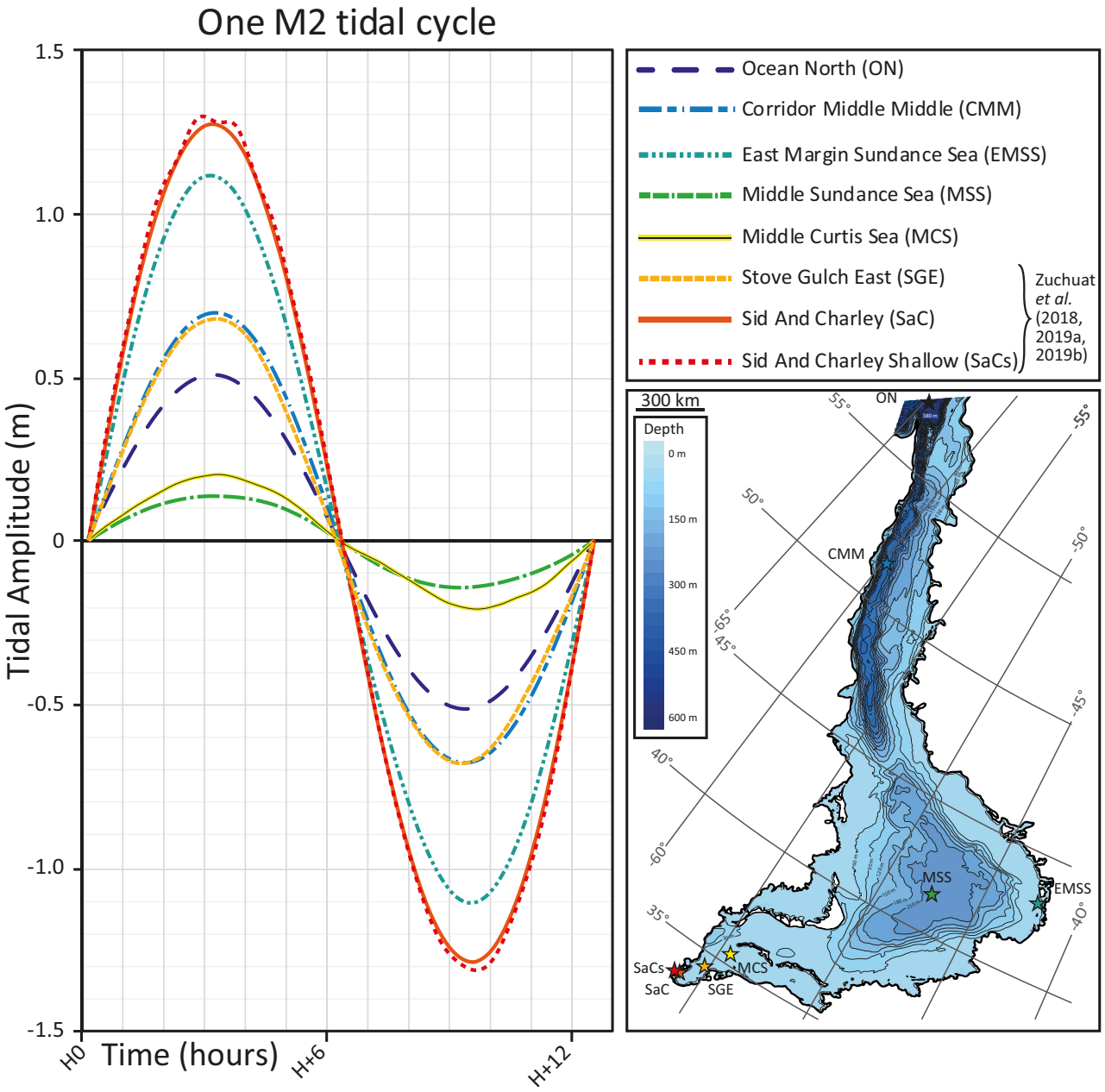

Fig. 4. Graph showing the simulated tidal amplitude (TA) over one M2 tidal cycle at eight key localities of the Sundance and Curtis seas, using the 600 m depth scenario. With an initial open-ocean tidal forcing of 0.5 m at the mouth of the system (ON), the tides are amplified by 162% in the inner parts of the Curtis Sea, reaching 1.31 m at Sid and Charley shallows (SaCs).

reaching equilibrium is likely linked to internally generated oscillations in the basin, but this analysis extends beyond the scope of this paper. An initial tidal amplitude of 0.5 m was applied at the model boundary at the mouth of the system (note that tidal amplitude values equal half the tidal range, which is the height difference between high tide and low tide). Similar to today, the Palaeo-Pacific Ocean was too large to host large tides (Green *et al.*, 2017; Laugie *et al.*, 2020), which is why this initial tidal amplitude of 0.5 m (supported by unpublished global simulations of the time slice), was selected. A higher tidal amplitude boundary condition of 2 m was also used to test how the basin would respond to changes in tidal forcing (Fig. 5). The

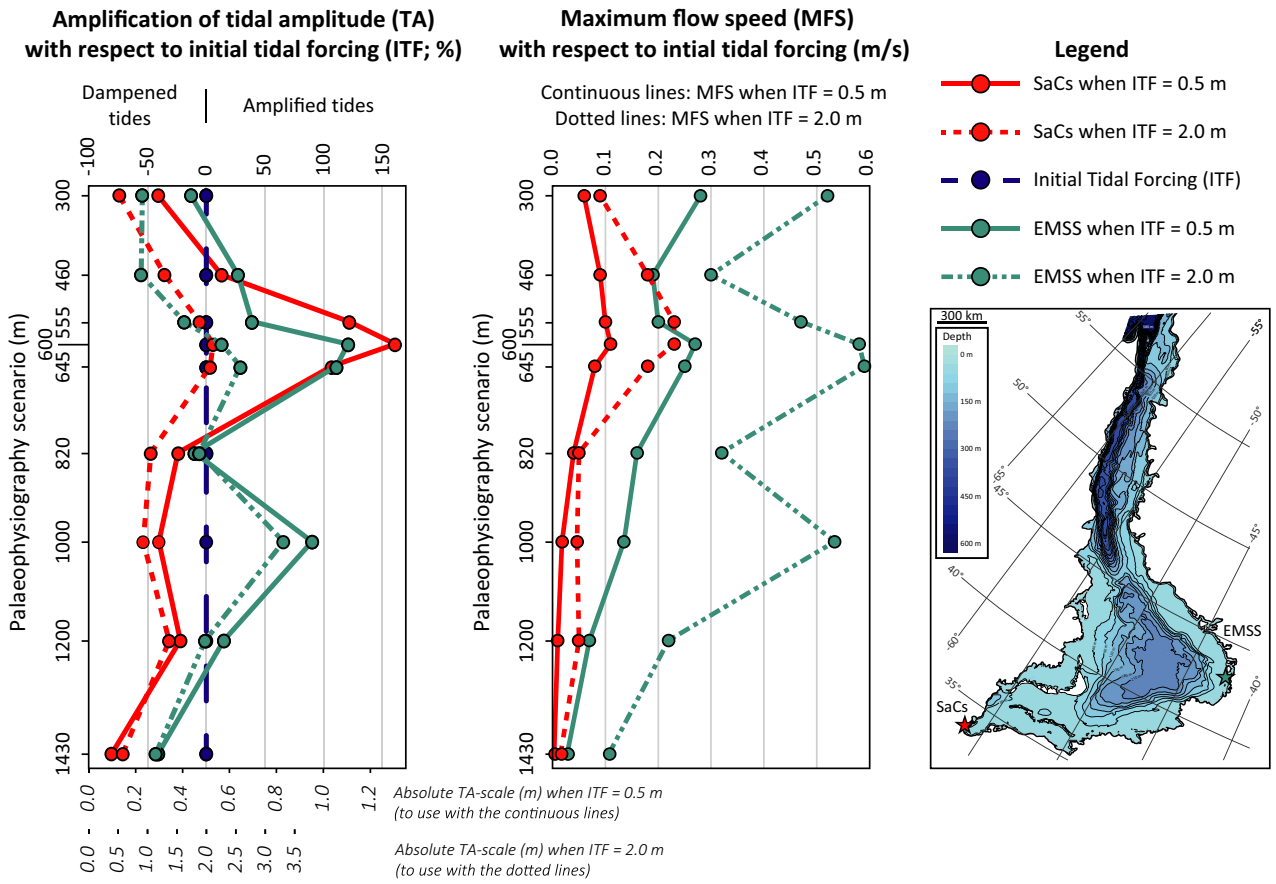

Sid and Charley Shallow (SaCs)

Depth scenario	Initial Tidal Forcing = 0.5 m			Initial Tidal Forcing = 2 m			Tidal Amplitude Increase Factor	Maximum Flow Speed Increase Factor
	Tidal Amplitude (m)	*% of Initial Tidal Forcing*	*Maximum Flow Speed (m/s)*	*Tidal Amplitude (m)*	*% of Initial Tidal Forcing*	*Maximum Flow Speed (m/s)*		
300 m	0.30	59.0	0.06	0.50	24.8	0.090	0.42	1.50
460 m	0.57	113.0	0.09	1.27	63.5	0.180	0.56	2.00
555 m	1.11	221.9	0.10	1.87	93.5	0.230	0.42	2.30
600 m	1.31	261.0	0.11	2.10	105.0	0.230	0.40	2.09
645 m	1.04	207.0	0.08	2.06	102.8	0.180	0.50	2.25
820 m	0.38	76.0	0.04	1.04	51.8	0.050	0.68	1.25
1000 m	0.30	59.5	0.02	0.90	45.2	0.047	0.76	2.58
1200 m	0.39	78.0	0.01	1.35	67.5	0.050	0.87	5.00
1430 m	0.10	19.1	0.003	0.55	27.7	0.015	1.45	4.97

East Margin Sundance Sea (EMSS)

Depth scenario	Initial Tidal Forcing = 0.5 m			Initial Tidal Forcing = 2 m			Tidal Amplitude Increase Factor	Maximum Flow Speed Increase Factor
	Tidal Amplitude (m)	*% of Initial Tidal Forcing*	*Maximum Flow Speed (m/s)*	*Tidal Amplitude (m)*	*% of Initial Tidal Forcing*	*Maximum Flow Speed (m/s)*		
300 m	0.44	87.0	0.28	0.89	44.5	0.520	0.51	1.86
460 m	0.64	127.0	0.19	0.87	43.5	0.300	0.34	1.58
555 m	0.70	139.0	0.20	1.61	80.5	0.470	0.58	2.35
600 m	1.11	221.0	0.27	2.25	112.5	0.580	0.51	2.15
645 m	1.06	211.0	0.25	2.57	128.5	0.590	0.61	2.36
820 m	0.45	90.0	0.16	1.87	93.3	0.320	1.04	2.00
1000 m	0.95	190.2	0.14	3.31	165.4	0.534	0.87	3.95
1200 m	0.58	115.0	0.07	1.97	98.3	0.220	0.85	3.14
1430 m	0.29	58.9	0.03	1.12	55.8	0.107	0.95	3.83

Fig. 5. Tidal amplitude (TA) and maximum flow speed (MFS) at Sid and Charley shallows (SaCs) and eastern margin of the Sundance Sea (EMSS) changing as a function of varying the initial open-ocean tidal forcing.

bed shear stress τ (Lentz *et al.*, 1999; Wells *et al.*, 2007) was calculated using:

$$\tau = \rho C_D \vec{u} \left| \vec{u} \right| \quad (1)$$

where ρ is the fluid density, $\vec{u}$ is the fluid velocity and C_D is the bottom drag coefficient. The simulations used a canonical drag coefficient (C_D) value of 0.002, derived from the default Chézy coefficient in Delft3D of C_z = 65 $m^{1/2}/s$ (Mulligan *et al.*, 2010) given by:

$$C_D = \frac{g}{C_z^2} \quad (2)$$

where, g is the gravitational acceleration. Equation 3 expresses the dissipation rate D (Taylor, 1920) and was calculated for each of the 18 simulations at every step of one complete tidal cycle:

$$D = \rho C_D \left| \vec{u} \right|^3 \quad (3)$$

where ρ is water density, C_D is the drag coefficient, and u is the speed of the current. Subsequently, a one-tidal-cycle-average dissipation rate was calculated for each model observation site in the Curtis Sea before being averaged across the Curtis Sea for each depth scenario (Table 1).

Using the 600 m depth scenario and a 0.5 m initial tidal forcing, two additional simulations were run using a high and a low C_D-value in order to test the sensitivity of the model to changes in the drag coefficient. The high C_D-value of 0.004 corresponds to C_z= 46 $m^{1/2}/s$; and the low C_D-value of 0.001 equates to C_z= 92 $m^{1/2}/s$.

In addition to the collection of basin-wide data at every step of the simulation (Figs 6 and 7), 34 artificial 'observation sites' were positioned in the model domain across the seas to monitor and collect water level, flow speed, and bed shear stress values, of which 16 representative sites (Fig. 1) were actively used to analyse simulation results. Of these 34 observation sites, eight are used here to highlight diagnostic behaviours of the tides across the basin (Figs 4 and 8). Note that the maximum water level amplitude across the domain (Fig. 6C) was computed by comparing 47 maps over 47 consecutive hours.

Table 1. Comparison between average dissipation values calculated for each palaeophysiographic configuration for a 0.5 m initial open-ocean tidal forcing and a 2.0 m open-ocean tidal forcing, showing that the dissipation rate is at least 11.5 times stronger with an initial tidal amplitude (TA) four times higher. This increase factor varies significantly and non-linearly, depending on the palaeophysiography.

Depth scenario	Basin-averaged D*, 0.5 m ITF	Basin-averaged D*, 2 m ITF	Increase factor
1430 m	0.00001	0.00076	54.56
1200 m	0.00028	0.00653	23.18
1000 m	0.00073	0.00879	12.11
820 m	0.00019	0.00701	37.51
645 m	0.00104	0.01242	11.96
600 m	0.00425	0.04915	11.55
555 m	0.00172	0.04310	25.11
460 m	0.00043	0.01057	24.44
300 m	0.00017	0.00729	43.96

ITF, Initial, open-ocean tidal forcing.
*Calculated using Eqs 1, 2 and 3.

SIMULATION RESULTS

Each of the nine palaeophysiographic configurations were used to run simulations with 0.5 m and 2.0 m initial tidal forcing, and an additional two simulations focused on changing C_D, resulting in a total of 20 simulations. This study focuses on the nine simulations run with an initial tidal forcing of 0.5 m (Figs 4, 6, 7 and 8). The results of the simulations run with an initial tidal forcing of 2 m are available as supplementary material (Appendix B).

Tidal characteristics, 600 m depth scenario

The simulation results of the 600 m depth scenario generated a distribution of simulated bed shear-stress in the Curtis Sea resembling the main observed grain-size distributions in the lower Curtis (*sensu* Zuchuat *et al.*, 2018; see discussion below). This palaeophysiographic configuration is also associated with the most amplified simulated tides, which matches well with the strong tidal indicators in the lower Curtis Formation. Therefore, the initial focus is on this scenario as the most likely to represent the conditions during deposition of the Curtis Formation in the earliest Oxfordian. In this scenario, the simulated tidal amplitudes showed a 10-minute tidal asymmetry in most of the basin, meaning that the ebb flow lasted 10 minutes longer than the flood flow (Fig. 4); it is only in the innermost parts of the Curtis Sea that this is not the case.

The tidal circulation in the central, southern and eastern Sundance Sea was centred on an

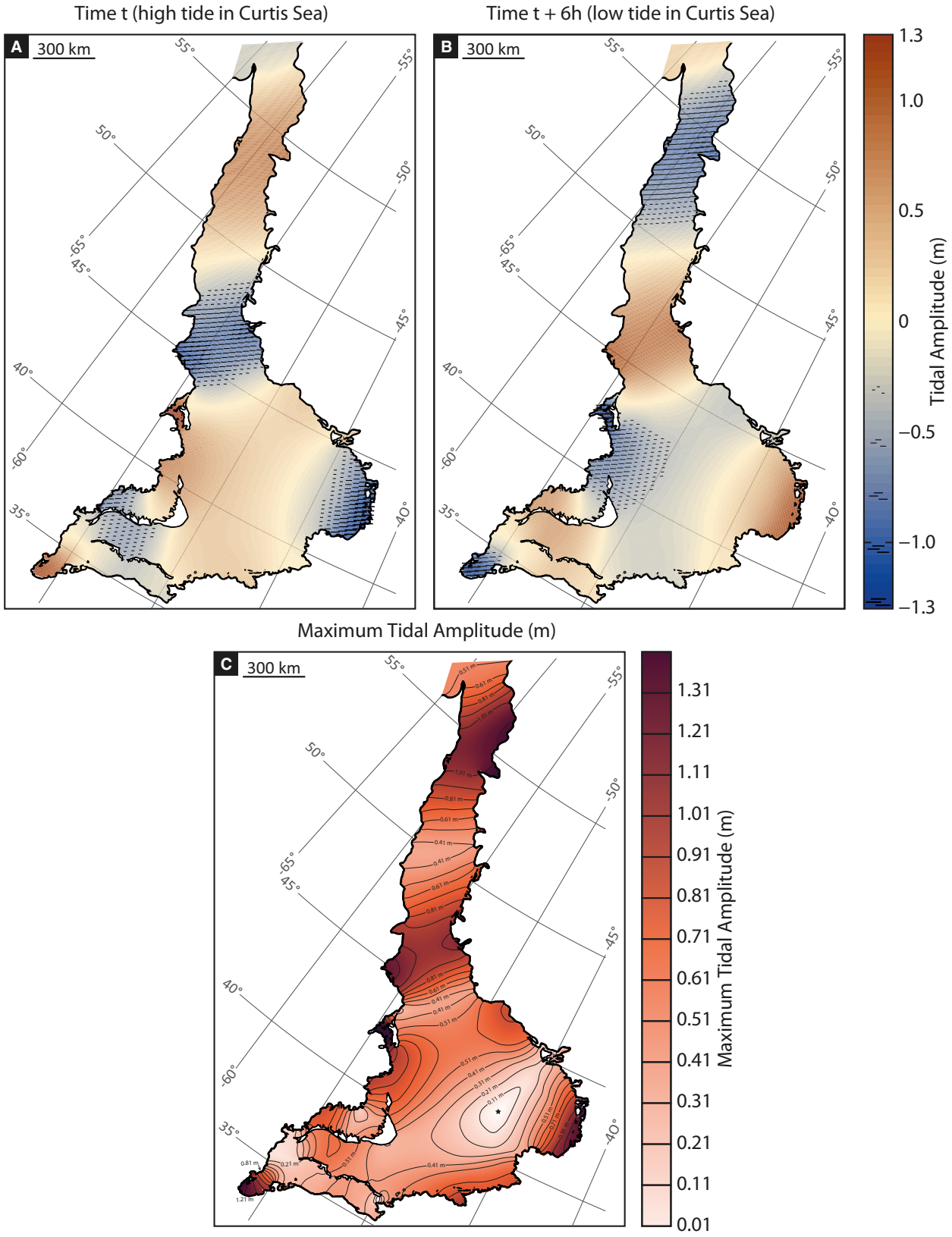

Fig. 6. Maps showing the distribution of the water level at time *t*, corresponding to (A) the high tide in the Curtis Sea, and (B) at time $t + 6$, corresponding to the low tide in the Curtis Sea, for the 600 m depth scenario, with an initial open-ocean tidal forcing of 0.5 m. (C) Map showing the distribution of maximum tidal amplitude (m).

amphidromic point (*ca* 46°W, 42°N; Fig. 6C; see also the animated abstract available with the online version of this manuscript). The area between the central Sundance Sea and the Curtis Sea comprised a number of islands and inlets that separated the main water body into various sub-basins (Fig. 1). This configuration of barriers and narrow openings strongly affected the tidal propagation and hindered the development of an amphidromic circulation, despite the dimensions of the basin theoretically permitting it, as the Rossby Deformation Radius at 35°N is close to the width of the Curtis Sea (Fig. 6; Zuchuat *et al.*, 2019b). The tides propagated in a rectilinear fashion along the long-axis of the Curtis Sea, which is confirmed by palaeocurrent observations from the Curtis Formation (Figs 7C and 9). High tide and low tide, as well as ebb tide and flood tide, have a very similar magnitude current flowing in the opposite direction.

The tides at both the Curtis Sea coastline and the eastern margin of the Sundance Sea (EMSS) had an amplitude more than twice that of the tidal forcing at the mouth (Figs 4 and 6), but they were out of phase: one region experienced high tides while the other experienced low tides (Fig. 6A and B). Although the tidal amplitudes simulated in both areas were similar (Fig. 6C), differences occurred in maximum flow speed and bed shear stress values during their respective ebb and flood tides (Fig. 7A and B). Both of these values were much higher in the bottleneck of the Curtis Sea (Stove Gulch East, SGE; Figs 7A, 7B and 8) than on the more open EMSS, indicating that the funnelling of the basin had a stronger impact on the simulated flow speed and the bed shear stress values than on the tidal amplitude. These results also indicate that most of the sediment transport in the Curtis Sea would occur during ebb tide and flood tides. Such spatial variations in flow speed and bed shear stress would be reflected in the rock record along the Curtis Sea coastline and the eastern margin of the Sundance Sea (EMSS), where different sediment grain sizes (Yalin & Karahan, 1979; van Rijn, 1993; Ward *et al.*, 2015, 2020) and different sedimentary architecture would occur (Hori *et al.*, 2002; Costas & FitzGerald, 2011; Sleveland *et al.*, 2020) despite similar tidal amplitudes.

The observation of out of phase tides between the Curtis Sea coastline in the west and the Sundance Sea margin to the east suggests the occurrence of a standing wave, associated with tidal resonance (*sensu* Sztanó & Boer, 1995), during which autogenic tidal processes can strongly impact the transport and deposition of sediments (Zuchuat *et al.*, 2019b). The simplest oscillation in a basin closed at both ends occurs when the water alternately falls and rises at each end with a nodal line across the centre, where there is no vertical motion (Allen, 1997). However, west to east 1.5 M2 tidal waves propagate in the Curtis–Sundance system in the widest, southern extent of the seaway (Fig. 6). The 1.5 wavelength harmonic is defined as:

$$T = 0.67L/\sqrt{gd} \quad (4)$$

with T being the M2 periodicity (44,712 s), g the gravitational acceleration (9.81 ms^{-2}), L = basin length (m; *ca* 1600 km from the edge of the Curtis Sea to the eastern margin of the Sundance Sea; Fig. 6) and d the average water depth. Solving Eq. 4 for the depth d indicates when the M2 wave will resonate with 1.5 wavelengths. This happens when the average water depth d is *ca* 60 m.

Change in palaeophysiographic configuration

Changes in palaeophysiographic configuration strongly affected the resulting simulated tidal amplitude, and hence the flow speed and associated bed shear stress in the basin (Fig. 8). Certain palaeophysiographic configurations resulted in an overall amplification of the initial tidal signal (for example, 555 m, 600 m and 645 m depth scenarios), whereas other palaeophysiographic configurations caused these parameters to be dampened (300 m, 820 m and 1430 m depth scenarios), or ever so slightly amplified for only a few localities (460 m and 1200 m depth scenarios). That is, the reactivity of the system to change in physiography was not uniform across the basin. The observation sites located in the central and deeper areas of the basin [Middle Sundance Sea (MSS) and Middle Curtis Sea (MCS)] recorded a more dampened tidal amplitude with respect to the initial tidal forcing in all simulations, and their response to change in physiography was less-pronounced than observation sites located closer to the shoreline. For instance, the coastal site at Sid and Charley (Fig. 1, SaC), showed strong changes in response to changing physiography. At Sid and Charley, tides were only slightly amplified with respect to the initial 0.5 m tidal forcing under the 460 m depth scenario, reaching tidal amplitude values of 0.56 m (Fig. 8; see also Appendix B). However, under the 600 m depth scenario, which resulted in a local increase in water depth of only *ca* 7.5 m and an increase in slope gradient

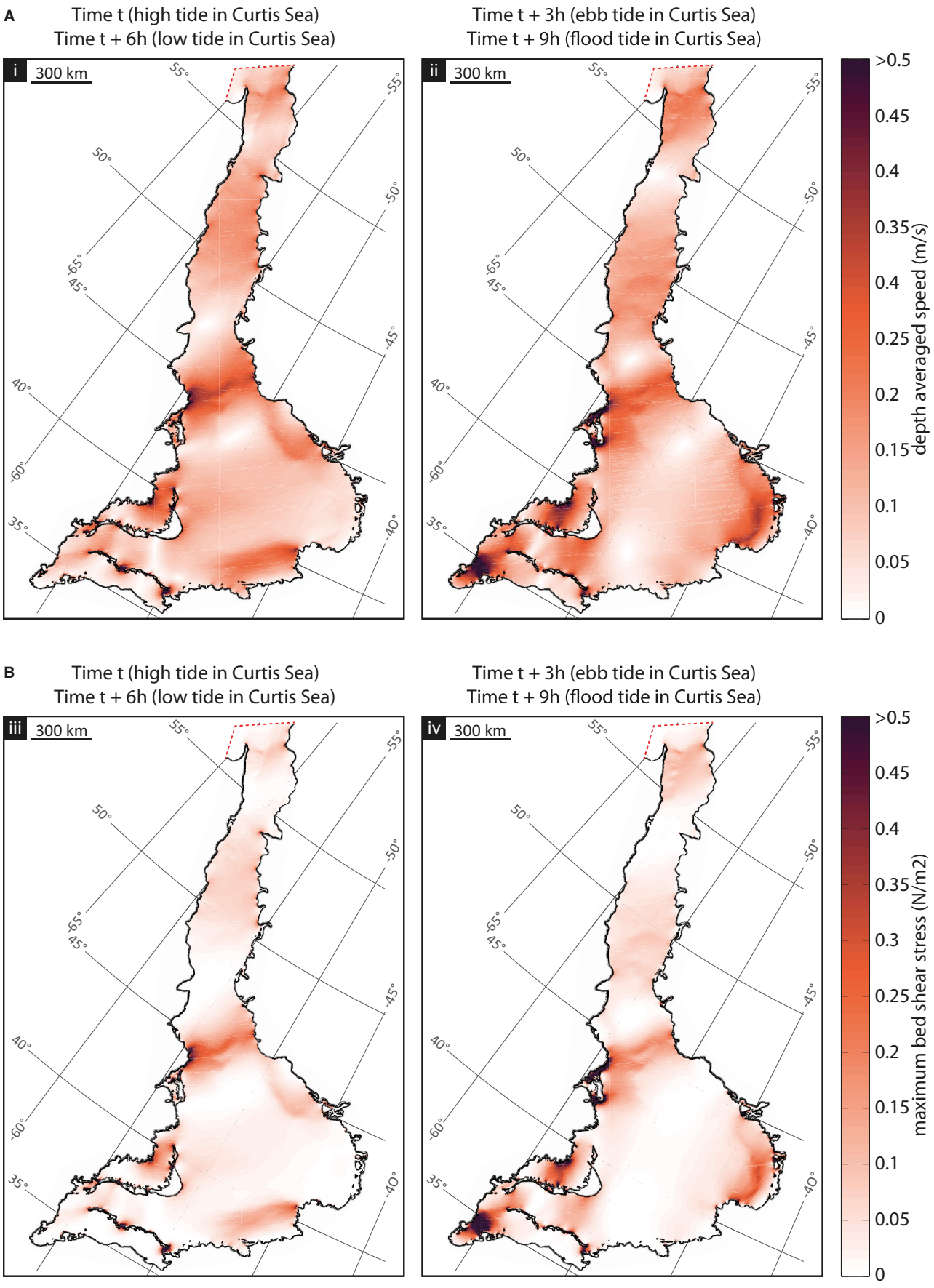

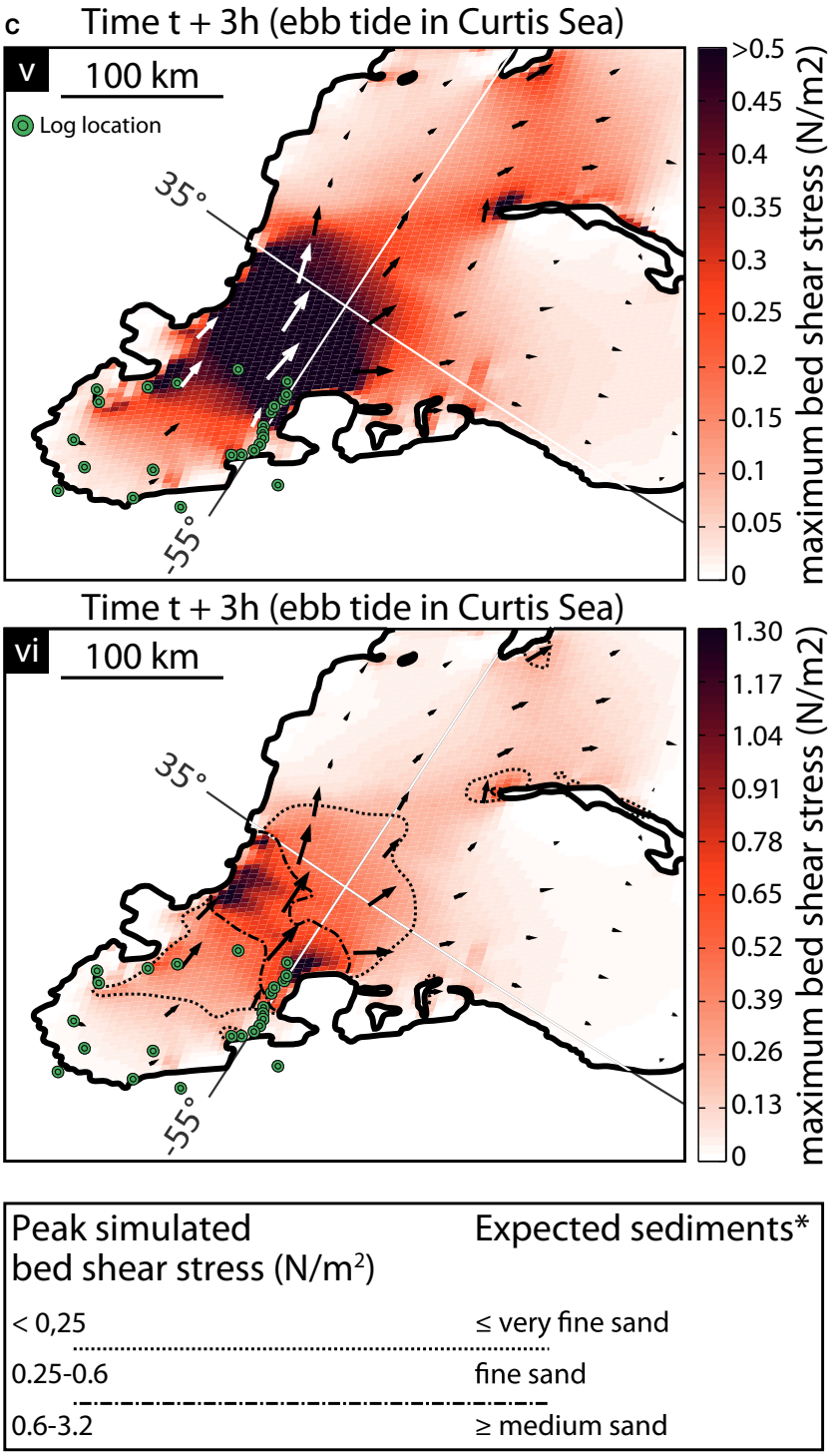

Fig. 7. Simulation results for the 600 m depth scenario. (A) Maps showing the distribution of the simulated depth-averaged speeds: (i) at time *t* and *t* + 6 (high tide and low tide in the Curtis Sea, respectively); and (ii) at time *t* + 3 and *t* + 9 (ebb tide and flood tide in the Curtis Sea, respectively). High tide and low tide were grouped together because they have a very similar magnitude with the opposite direction, and ebb tide and flood tide have been grouped together for the same reason. (B) Maps showing the distribution of the simulated bed shear stress values: (iii) at time *t* and *t* + 6 (high tide and low tide in the Curtis Sea, respectively); and (iv) at time *t* + 3 and *t* + 9 (ebb tide and flood tide in the Curtis Sea, respectively). (C) Zoomed-in view of the Curtis Sea, showing (v) and (vi) the distribution of the simulated bed shear stress values using two different scales at time *t* + 3 (ebb tide in the Curtis Sea) with vector arrows, as well as the locations of sedimentary logs displayed in Fig. 9. Expected sediments modified after Ward *et al.* (2015).

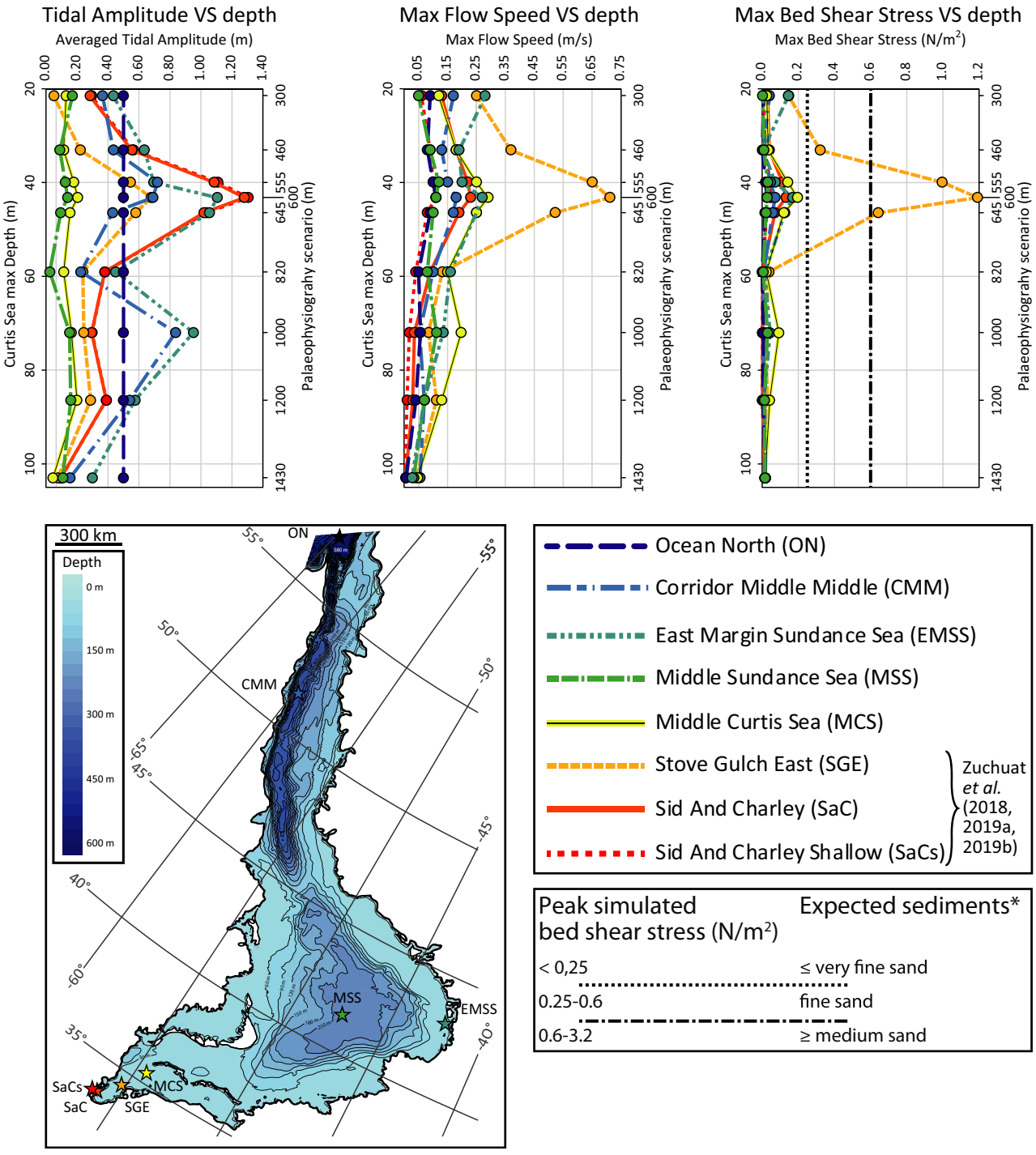

Fig. 8. Simulated maximum tidal amplitudes, flow velocities and bed shear stress at eight key localities for each modelled palaeophysiographic configuration, with an initial open-ocean tidal forcing of 0.5 m at the mouth of the system (ON). Expected sediments modified after Ward *et al.* (2015).

of 0.006°, tides were amplified to 1.28 m. Not all coastal areas responded to change in physiography in a similar manner, illustrated by the results of the 1000 m depth scenario (Fig. 8). This palaeophysiographic configuration led to spatial separation of the tidal amplification in the basin: the tidal amplitude at the eastern margin of the Sundance Sea (EMSS) was nearly

twice the value of the initial tidal forcing, whereas the tidal amplitude in the Curtis Sea was reduced to nearly half the value of the initial tidal forcing. Despite an increased tidal amplitude, the 1000 m depth scenario did not lead to increased flow speed and associated bed shear stress values at the EMSS. Consequently, changes in palaeophysiography controlled both the magnitude and the location of tidal amplification, as well as flow speed and bed shear stress variations in the basin. This shows the importance of physiography on regional tidal dynamics and further supports the large-scale results of Blackledge *et al.* (2020), who showed that tidal dissipation rates are fundamentally controlled by the distribution of continental masses and associated ocean bathymetry around the globe, and the tidal dissipation rates will vary through geological time as a consequence of plate tectonics (Green *et al.*, 2018).

Steps between palaeophysiographic configurations represent increases in both water depth and seafloor gradient. Results of these simulations suggest how the system would respond to relative sea-level variations, using the steps between each depth scenario as a proxy for relative sea-level change (Fig. 8) given that the seafloor deforms due to the water column weight variation [self-attraction and loading (SAL) effect; e.g. Gordeev *et al.*, 1977; Richter *et al.*, 2013; Apecechea *et al.*, 2017; although the SAL effect would be greatly exaggerated here]. Starting with the shallowest basin configuration (i.e. the 300 m depth scenario), tides first become amplified as the relative sea level increases, until the system reaches a palaeophysiographic configuration (the 600 m depth scenario) for which the tidal amplitudes are at a maximum, especially in shallow areas close to the coastline. As relative sea-level rise continues, the tidal amplitude subsequently diminishes everywhere in the basin. The deeper the basin becomes, the more heterogeneous the spatial distribution of the tidal amplitude is, resulting in different periodic resurgence of tidal amplification or dampening (Fig. 8). As a result, the hydrodynamics and resulting sedimentary deposits would strongly vary from one side of the basin to the other, despite a similar relative sea-level history.

Change of initial tidal forcing

The simulations also explored the effects of varying tidal forcing at the open boundary from 0.5 m to 2.0 m, illustrated by data from SaCs and EMSS (Fig. 5; see Appendix B). The simulations were sensitive to changes in initial tidal forcing, but each location responded differently to these variations, as illustrated by the various increase factors (Fig. 5). Under a 555 m depth scenario, an initial tidal forcing of 0.5 m resulted in 122% amplification of the tides at SaCs, whereas initial forcing of 2 m resulted in 6% dampening of tides (Fig. 5). This means that, under a 555 m depth scenario, the amount of amplification at SaCs increased by a factor of 0.42 when augmenting the initial tidal forcing from 0.5 to 2.0 m. Contrastingly, at EMSS, this increase factor equalled 0.58. In other words, the tidal amplitude at both locations diminished, but it diminished differently when changing the initial tidal forcing from 0.5 to 2.0 m. Furthermore, the values of these increase factors changed non-linearly when running the simulations with a different palaeophysiographic configuration, and each locality followed a different, non-linear trend (Fig. 5).

The evolution of the relationship between the tidal amplitude and the flow speed with respect to changes in palaeophysiography is complex (Fig. 5) and requires incorporation of additional factors which go beyond the scope of this study to fully decipher the true link between the tidal amplitude and the associated flow speed. At SaCs, when using an initial tidal forcing of 0.5 m, both 1000 m and 300 m depth scenarios experienced a similar tidal amplitude. However, the associated flow speed was three times higher in the 300 m depth scenario than the 1000 m one. This discrepancy in flow speed was due to the different cross-sectional area of the basin between the depth scenarios: in both simulations, the same volume of water had to flow in the same amount of time. The simulated flow speed experienced using the 300 m depth scenario was three times higher than that experienced using the 1000 m depth scenario because the cross-sectional area was three times smaller.

Dissipation rate, *D*

Table 1 illustrates how the dissipation rate, *D,* may likely have evolved in the Curtis Sea as a function of initial tidal forcing and palaeophysiographic configuration. Overall, an increase in initial tidal forcing always resulted in a higher rate of dissipation in the Curtis Sea, regardless of the palaeophysiographic configuration, because *D* was calculated using Eq. 3. Because the use of different

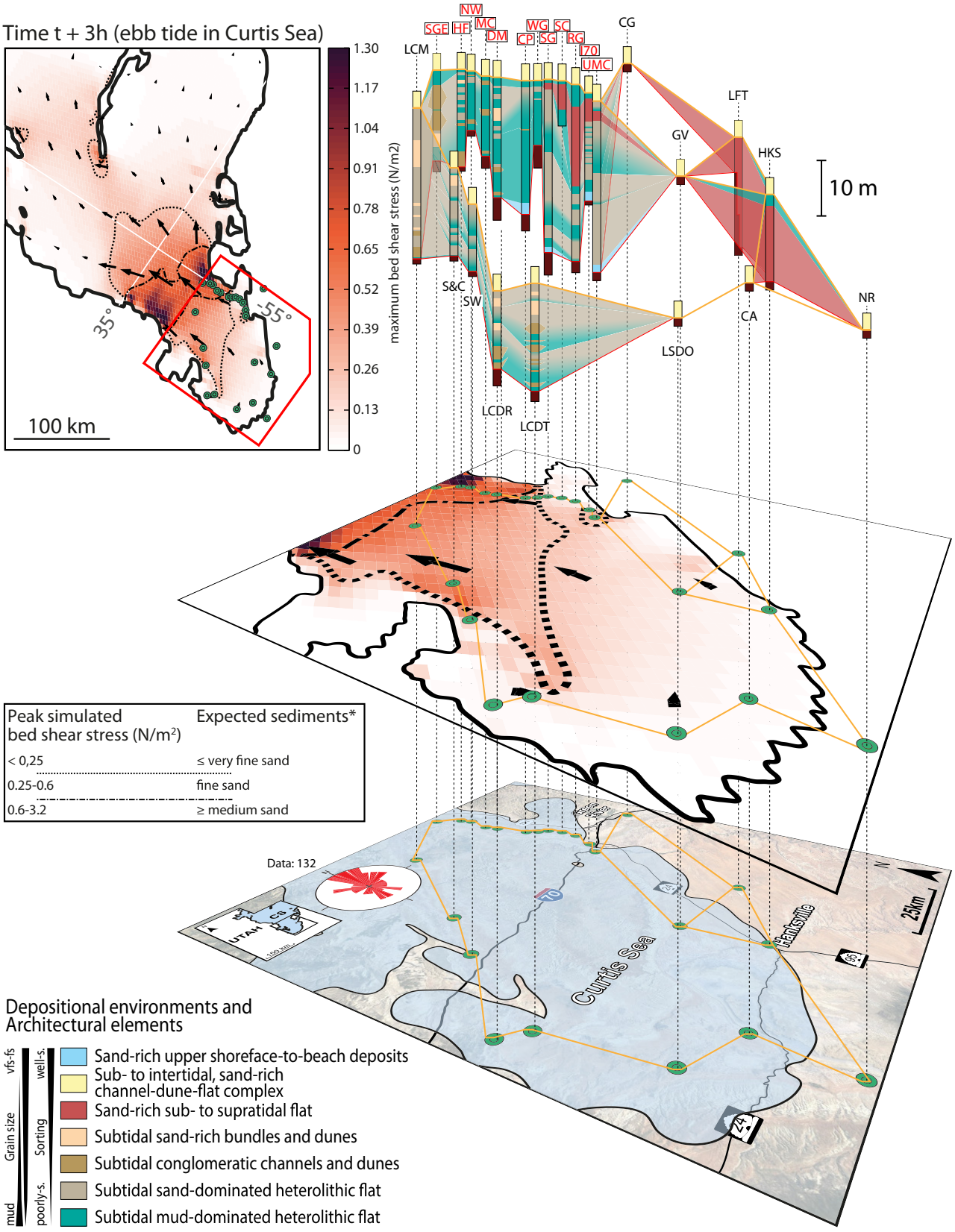

Fig. 9. Fence diagram showing the distribution of the different facies associations and prominent architectural elements in the lower Curtis, draped onto the maximum-bed-shear-stress map at time $t + 3$ (ebb tide in the Curtis Sea), and simplified palaeogeographical map of the Curtis Sea. The rose diagram indicates measured palaeocurrent direction in the lower Curtis. Location abbreviations, from the north, clockwise: SGE, Stove Gulch East; HF, Humbug Flats East; NW, Neversweat Wash; MC, Middle Canyon; DM, Dry Mesa; CP, Curtis Point; WG, Wet Gulch; SG, Sven's Gulch; SC, Smith's Cabin; RG, Rabbit Gulch; I70, Interstate 70; UMC, Uneva Mine Canyon; CG, Crystal Geyser; GV, Goblin Valley; LFT, Little Flat Top; HKS, Hanksville; NR, Nottom Ranch; CA, Caineville Airstrip; LSDO, Lower South Desert Overlook; LSDT, Last Chance Desert Tower; LSDR, Last Chance Desert Road cut; SW, Saltwash View Area; SaC, Sid and Charley; LCM, Lower Cedar Mountain. Locations in red are displayed in a more detailed correlation panel in Fig. 10. Expected sediments after Ward *et al.* (2015).

palaeophysiographic configuration impacted the flow speed at each location (Appendix B), the resulting *D*-value of the Curtis Sea varied between simulations. Furthermore, since these changes in speed varied in a non-linear fashion as cross-sectional dimension varied, but not the volume of water to be moved (Fig. 5; see also Appendix B), the changes in dissipation rate *D* evolved non-systematically as the palaeophysiography changed.

Change in drag coefficient

Changing the drag coefficient parameter, C_D, impacted the modelled tidal amplitude, flow speed and bed shear stress values (Appendix C): lower C_D resulted in higher tidal amplitude and higher flow speeds. This relationship was not observed in the bed shear stress, which followed three different trends because of its interdependence on C_D and the speed, Eq. 3. As C_D increases, the bed shear stress either: (i) increases; (ii) increases then decreases; or (iii) decreases. These three trends were distributed systematically across the basin: the increasing trend was recorded from the mouth of the system into the main body of the Sundance Sea, whereas the increase–decrease and the decrease trends only occurred in the Curtis Sea.

DISCUSSION

Model validation and implication for regional palaeogeography

The lowermost interval of the shallow-marine Curtis Formation (lower Curtis, *sensu* Zuchuat *et al.*, 2018) in east-central Utah is characterized by coarser sediments and more sand-dominated strata in the north-east and north-west areas, whereas regions to the south generally display finer-grained, more thinly-bedded, and more heterolithic beds (Figs 9 and 10). This distribution of sedimentary facies and facies associations, when placed in a palaeogeographical context, shows that the coarser sediments were deposited in the bottleneck near Stove Gulch East (SGE; Fig. 1), as well as along the north-west shoreline of the Curtis Sea, whereas finer sediments were deposited in the innermost parts of the Curtis Sea to the south.

As an idealized approximation, simulated bed shear-stress values can be used as a proxy to estimate the different grain sizes of the sediments deposited by tidal processes (Ward *et al.*, 2015, 2020), with higher bed shear stress corresponding to coarser sediments (Fig. 9). The distribution of the bed shear-stress values during ebb and flood tides in the Curtis Sea for the 600 m depth scenario (Fig. 7C) showed a very similar trend to the observed grain-size distributions in the lower Curtis. The highest bed shear stress values were concentrated at the bottleneck near Stove Gulch East (SGE; Fig. 1) and along the north-west shoreline of the system. The innermost parts of the Curtis Sea were characterized by lower bed shear-stress values, which corresponds well with finer-grained sediments observed in outcrop (Figs 9 and 10). A better-resolved bathymetry will have an impact on the values and the distribution of the bed shear stress in the model, but given the regional nature of the modelled tides and the physiography of the basin, the matching trends between the simulations and the rock record will most likely remain the same.

The model did not match all outcrop localities. Although the model could explain the sedimentary architecture of the lower Curtis in the northern and western parts of the study area, it failed to explain the southward-coarsening trend observed in outcrop towards the innermost parts of the Curtis Sea (Figs 9 and 10). The model predicted that the sediments in these southern areas could not be coarser than very fine sand (Figs 7C, 9 and 10), but the lower Curtis in these southern areas consists of mostly thinly-bedded

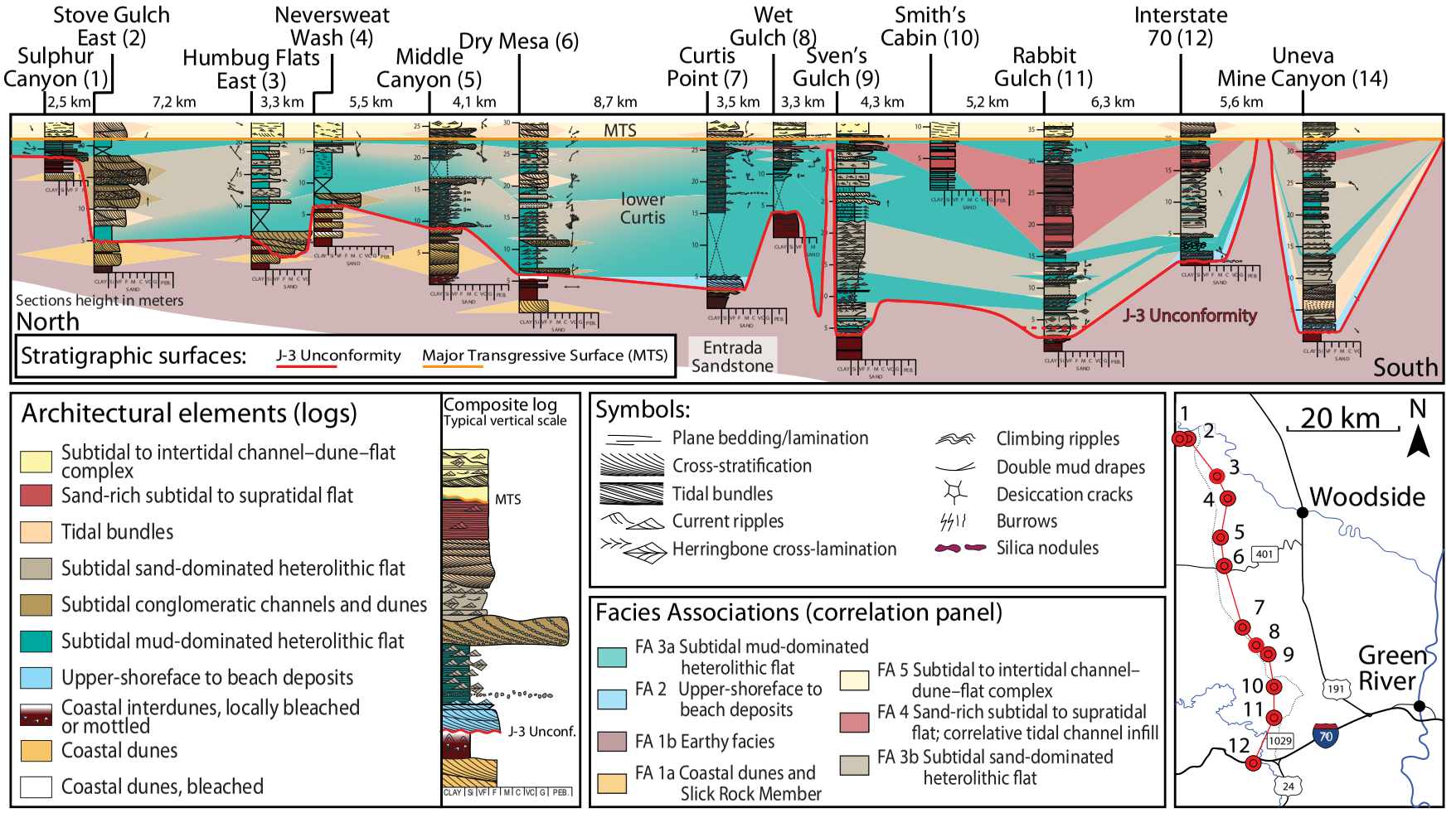

Fig. 10. Correlation panel of the lower Curtis across the north-east margin of the San Rafael Swell, showing the distribution of facies associations (see Zuchuat *et al.*, 2018, for detailed sedimentological descriptions).

fine-grained sandstones (Figs 9 and 10) with diagnostic tidal signatures (Kreisa & Moila, 1986; Caputo & Pryor, 1991; Wilcox & Currie, 2008; Zuchuat *et al.*, 2018). Such discrepancies between the simulated sediment distribution and the geological record in the southern areas of the Curtis Sea could be an artefact of the model's simplicity, which only integrated the M2 tidal constituent, as well as a grid-resolution too big to render the effect of the precise coastal geometry, small islands (see discussion in Green & Pugh, 2020) and morphological features developing on the seafloor (dunes, bars, troughs, channels, etc.). Whilst M2 was often the dominant constituent, and adding other constituents tends not to drastically alter the conclusions of a study (e.g. Wells *et al.*, 2007, 2008), incorporating diurnal tidal constituents (K1 and O1) could have slightly refined the distribution of the bed shear stress in the model. Diurnal constituents were potentially elevated at the connection with the open ocean, as observed today along the western coast of North America (tidal amplitude of *ca* 1.0 m and 0.45 m for M2 and K1, respectively) and simulated for an Aptian palaeogeography (Wells *et al.*, 2010). Furthermore, variations in clay content and quantity of extracellular polymeric substances would have impacted the nature and separation of the flow (Baas *et al.*, 2019; Wang *et al.*, 2019), as well as the distribution of sediment and bedforms in the system. Integrating these additional factors to the simulations, as well as increasing the grid resolution, might help to reduce the existing discrepancies between the model and the Curtis Formation, especially at a local scale (e.g. Azhikodan & Yokoyama, 2018). General trends, however, are expected to remain relatively constant, even with the addition of more complex input parameters.

Differences between the geology and the model could also suggest that sediment in the innermost parts of the Curtis Sea was transported and deposited by other processes (for example, wind or flash floods; Anthony *et al.*, 2010; Blanchard *et al.*, 2016; Rivers *et al.*, 2020), but whose signatures were not preserved in the rock record. Indeed, small relative sea-level changes in low-gradient basins lead to the migration of facies belts over large horizontal distances (Midtkandal & Nystuen, 2009; van Yperen *et al.*, 2019). The effects associated with the migration of the facies belts can be further amplified in arid, paralic environments, when these relative sea-level variations are associated with arid–humid climatic oscillations (Mountney, 2006; Anthony *et al.*, 2010; Jordan & Mountney, 2010, 2012; Blanchard *et al.*, 2016; Vieira & dos Santos Scherer, 2017). Increased periods of aridity facilitate the deposition and progradation of sand flats and aeolian dunes, which can subsequently be reworked by tidal currents as the sea transgresses the previously-exposed coastal areas (Anthony & Dobroniak, 2000; Anthony *et al.*, 2010).

The duration of each model run in this study is on the scale of months, whereas the lower Curtis Formation was deposited over tens of thousands of years. The model therefore represents a potential snapshot in time rather than a complete stratigraphic simulation. The relationships between short-lived sedimentary processes and their preservation in the sedimentary record is a debate that has persisted throughout sedimentological studies (e.g. Ager, 1973; Jerolmack & Sadler, 2007; Smith *et al.*, 2015, and references therein; Davies & Shillito, 2018; Paola *et al.*, 2018). However, the aim of the present study is simply to ask whether tidal simulations can be used to support geological observations and to explore the general effects of changing basin physiography on tidal processes. The stratigraphic record is never a complete record of basin history, but there is evidence for strong tides in the rock record (Kreisa & Moila, 1986; Caputo & Pryor, 1991; Wilcox & Currie, 2008; Doelling *et al.*, 2013; Zuchuat *et al.*, 2018), which the models presented here are able to resolve. A stratigraphic forward modelling exercise could explore a more detailed view of changing basin physiography and the associated depositional processes through time. However, this type of analysis is outside the scope of the present study, and would face limitations due to the poor chronostratigraphic control on the lower Curtis and the other coeval sedimentary units deposited towards the Sundance Sea. Despite the simplicity of the model presented here, the depositional energy near the Stove Gulch East bottleneck (SGE; Fig. 1) and along the north-west shoreline of the system remained stronger than depositional energy in the innermost parts of the Curtis Sea when the lower Curtis was being deposited, given that coarsest sediments in the lower Curtis are concentrated in the former areas, while finer-grained sediments were deposited in the latter (Figs 9 and 10). This means that a simplified tidal modelling exercise can pick up general depositional trends and could therefore be used to explore hypotheses proposed from the study of the rock record.

As absolute water-depth information is lacking for the Sundance and Curtis seas, the authors propose that the 600 m depth scenario could be considered a realistic depiction of the basin configuration during the earliest Oxfordian when the lower Curtis was being deposited, based on the simulation results and the similarities between the modelled sedimentary proxies and the lower Curtis depositional trends. The Sundance Sea would have therefore reached a maximum depth of *ca* 240 m, and the seafloor of the Curtis Sea would have laid 40 to 45 m below the surface. In this context, the 2.60 m tidal range of the Curtis Sea would classify it as a meso-tidal system.

Comparison to modern systems

While there are no modern analogues of the epicontinental Sundance and Curtis seas in terms of both size, setting and neighbouring climate belts, some basins and shallow seas today might display similar physiography. The Hudson Bay in Canada, for example, reaches a maximum depth of *ca* 200 m (Prinsenberg, 1986; Kuzyk *et al.*, 2008), with the highest tides occurring near Churchill and near the mouth of the Nelson River on the south-west margin of the Bay (>1.25 m; Prinsenberg & Freeman, 1986; Webb, 2014), opposite the connection between the bay and the Hudson Strait, resembling what has been modelled in the EMSS (Figs 5 and 6). Like the results herein, the tides in the Hudson Bay were shown to be extremely sensitive to sea-level change (Hayden *et al.*, 2020). The present-day North Sea, which is mostly shallower than 100 m but reaches depths of 300 m (Bockelmann *et al.*, 2018), provides another useful analogue with similar bathymetric ranges to our 600 m depth scenario. The North Sea has sandy sediment and tidal ridges towards the west and south, and muddy sediment towards the centre (e.g. Bockelmann *et al.*, 2018). Such sediment and bedform distribution reflect an amplification of tides towards the west and south, with three M2 and one K1 amphidromic points, together with slightly deeper water located towards the centre–east of the sea (e.g. Sinha & Pingree, 1997).

Impact on sequence stratigraphy of tide-dominated basins

The spatial distribution of sedimentary facies in tide-dominated environments is usually characterized by the deposition of finer-grained sediments along the coastline and coarser sediments at greater water depth, where current velocities and associated bed shear stress are higher (Dalrymple *et al.*, 2012; Fan, 2012). Fining-upward sedimentary successions are therefore typically interpreted to record coastal progradation in tidal systems. However, this assumes that the tidal dynamics in the system remain constant, despite changes to basin physiography. This study highlights how changing basin physiography can have a major impact on tidal dynamics, which should be considered when interpreting tidal stratigraphy. In this case, changing basin physiography, which includes basin gradient and water depth, was used as a proxy for sea-level change. To explore this further, a hypothetical sedimentary log is considered, with a lower coarsening-upward interval overlain by a fining-upward succession (Fig. 11; referred to as one 'CU2FU' package). The lower CU-interval records increasing depositional energy with time, with increasing tidal amplitude, flow speed and bed shear stress values, while the upper FU interval records a period of decreasing depositional energy with time. Classic tidal facies models (Dalrymple *et al.*, 2012; Fan, 2012) would interpret a waxing to waning energy trend as a transgression followed by regression, driven by either sea-level fluctuations or changes in sediment supply. Although variations in sediment supply would add an extra dimension to the complexity of the problem, this discussion was simplified by focusing on potential patterns driven solely by relative sea-level fluctuations. Results of the simulations presented in this study (Fig. 8) indicate that a coarsening to fining-upward trend could reflect four different relative sea-level histories: (i) a relative sea-level rise-then-fall cycle (Fig. 11C; or a relative sea-level rise followed by a period of relative sea-level standstill associated with coastal progradation); (ii) a relative sea-level fall-then-rise cycle (Fig. 11D); (iii) a constant relative sea-level rise (Fig. 11A); (iv) or a constant relative sea-level fall (Fig. 11B). In the last two cases, the coarsest sediments would have been deposited when the physiography of the basin reached an optimal configuration that maximized tidal amplification, flow speed and associated bed shear stress, potentially even reflecting the development of a resonant stage. Consequently, such a sedimentary succession is non-unique (*sensu* Burgess & Prince, 2015), because several different relative sea-level histories could produce the same pattern. Future

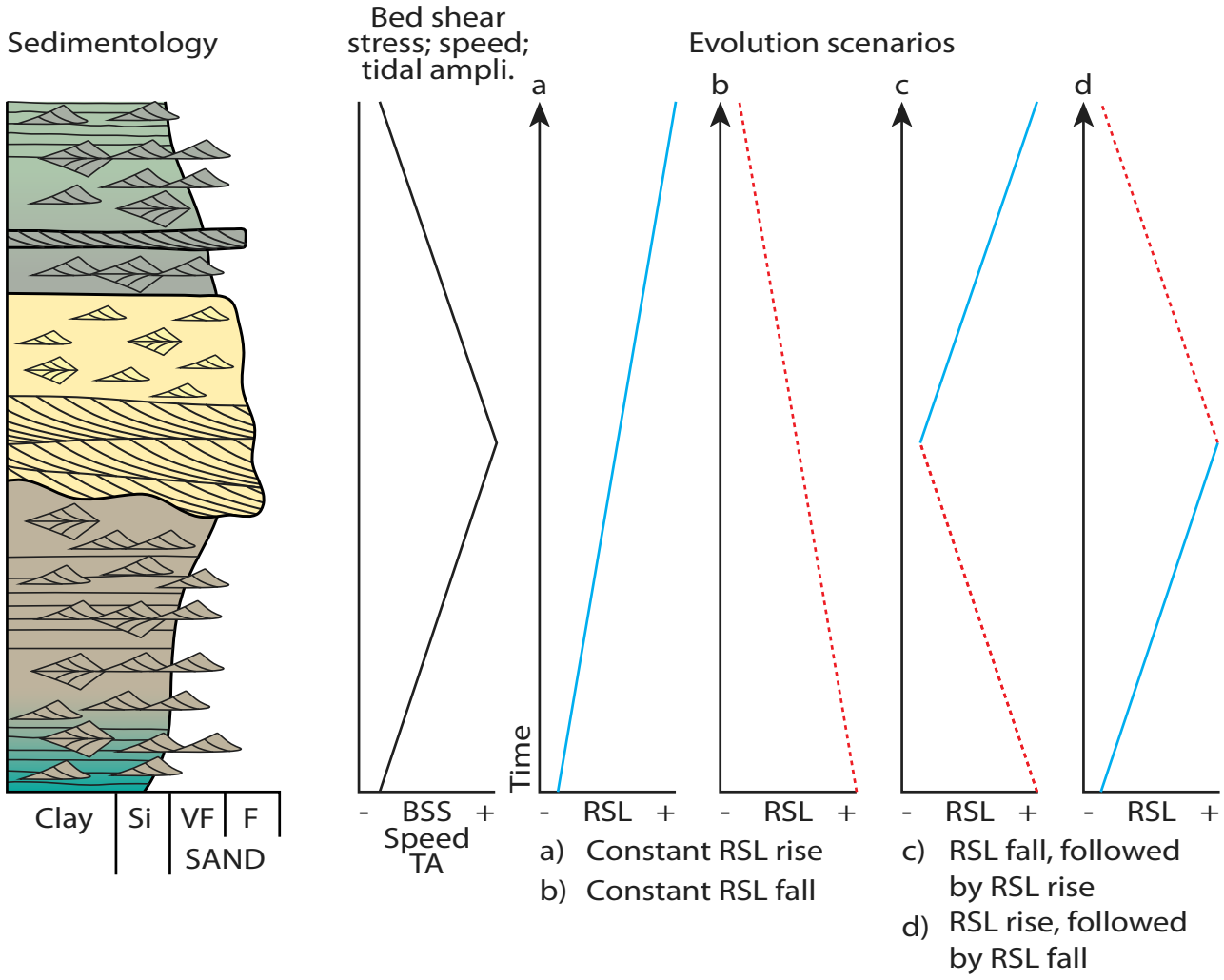

Fig. 11. Schematic log of a hypothetical tide-dominated sedimentary succession from Sid and Charley shallows (SaCs), showing a coarsening-upward trend, followed by a fining-upward trend. According to the simulation results, the sedimentology alone, in a tide dominated environment, does not reflect a specific relative sea-level (RSL) history. Four different RSL scenarios can lead to the same sedimentological column. BSS, bed shear stress; TA, tidal amplitude.

work will help to improve the understanding and the recognition of the transition from a non-resonant to a resonant stage in ancient, tide-dominated systems such as the Curtis Sea.

Under conditions of constant sea-level rise, the SaCs location in the Curtis Sea (Fig. 1) would record a succession similar to the hypothetical 'CU2FU' succession described above (Fig. 11). However, this same constant sea-level rise would have resulted in the deposition of two CU2FU packages overlying one another in the EMSS (Fig. 1) because that part of the basin would have reached a resonance-prone configuration twice given the occurrence of localized tidal harmonics (Fig. 8). Note that such a hypothetical section from the EMSS could reflect up to 16 different relative sea-level histories. This exercise is non-trivial, because it illustrates the fact that, in a basin in which tides are one of the dominant hydrodynamic processes, one particular relative sea-level history will result in the deposition of different sedimentary successions in different parts of the basin despite similar water depth, because they will reach a resonant-prone configuration at different moments in the basin's history. Consequently, in a tide-dominated basin, it is possible to consider relative sea-level change and its effect(s) as non-unique (*sensu* Burgess & Prince, 2015).

Greenberg *et al.* (2012) and Arns *et al.* (2015) showed that even a minor increase in relative sea level leads to a non-linear change in tidal amplitude combined with an altered tidal energy dissipation, especially in coastal areas close to tidal resonance. However, these changes are expressed differently depending on how the local physiography, the associated dissipation of tidal energy, and resonance properties of the basin evolve with respect to relative sea-level fluctuations (Ward *et al.*, 2012; Pelling *et al.*, 2013; Carless *et al.*, 2016; Idier *et al.*, 2017). The simulation results confirm that the Sundance and Curtis seas would have experienced the same spatial-dependence of tidal process variations with respect to changing basin physiography (Fig. 8). Thus, it is essential to consider distinct interpretations when investigating the evolution of a palaeo-sea in which tides were one of the main processes influencing the distribution and the deposition of sediments. The interpretation of the relative sea-level and sediment flux variations recognized in the stratigraphy could be refined and strengthened by the integration of additional proxies, including ichnology, clay mineralogy or bedform dynamics.

CONCLUSIONS

Recent research on modern tidal environments highlights the complexity of tidal systems (Dalrymple *et al.*, 2012; Fan, 2012; Gugliotta *et al.*, 2017; Cosma *et al.*, 2020; Finotello *et al.*, 2020). This increased understanding of modern systems is one way to improve the recognition and the interpretation of ancient tides (see discussion in Gugliotta & Saito, 2019). In addition to including insight from modern environments, numerical modelling (Collins *et al.*, 2018, 2021) can help to test hypotheses formulated from the study of the rock record and to tune ancient tidal signals to astronomical parameters, which have changed through time (Green *et al.*, 2017, 2018; Davies *et al.*, 2020).

The use of numerical modelling of the Upper Jurassic Sundance and Curtis seas allowed for constraints on and quantification of the formative tidal processes that could have formed interpreted tidal characteristics observed in the Upper Jurassic Curtis Formation (Kreisa & Moila, 1986; Caputo & Pryor, 1991; Wilcox & Currie, 2008; Doelling *et al.*, 2013; Zuchuat *et al.*, 2018, 2019a,b). Furthermore, numerical modelling also documented the influence of varying palaeophysiographic configuration, initial tidal forcing and bed shear stress values on the behaviour of M2 tides across epicontinental seas.

In the present study, tidal simulations showed that changes in physiography controlled the magnitude and the location of tidal amplification, flow speed and bed shear stress variations in the basin. These variables were also impacted by changes in initial tidal forcing and bottom drag coefficient, although to a lesser extent than changes in physiography.

The pattern of modelled tidal bed shear stress obtained using the 600 m depth scenario predict a distribution of sedimentary facies similar to those observed in the lower Curtis Formation, except in the southernmost parts of the Curtis Sea, close to the palaeoshoreline, where sediments might have been transported from the neighbouring arid coastal plain by aeolian processes and subsequently reworked by tidal currents. The 600 m depth scenario can therefore be considered a realistic palaeophysiography for the Sundance and Curtis seas. In this case, the Sundance Sea would have reached a maximum depth of *ca* 240 m, and the seafloor of the Curtis Sea would have reached maximum depth of 40 to 45 m. In this context, the simulated 2.60 m tidal range of the Curtis Sea would classify it as a meso-tidal system (2 × 1.30 m tidal amplitude).

Finally, sedimentary successions deposited in tide-dominated basins reflect the energy level (bed shear stress) and the degree of tidal amplification (or dampening) that prevailed at the time of deposition. Because these energy variations can be the product of several, equally-valid relative sea-level variations leading to the onset and cessation of tidal resonance during which autogenic tidal processes can strongly impact the transport and deposition of sediments (Zuchuat *et al.*, 2019b), the resulting sedimentary successions deposited under enhanced (or dampened) tidal energy could be considered non-unique (*sensu* Burgess & Prince, 2015). The present study also found that a given relative sea-level curve can lead to distinctive stacking patterns in different parts of a basin because of localized tidal harmonics, which implies that the impact of relative sea-level changes on stratigraphy are also non-unique. Consequently, interpretative caution is required and several possible interpretations should be considered when developing a geological model of a palaeo-sea, especially if tides were a dominant process. Additional proxies should be considered to robustly interpret the true relative sea-level variations recorded within

tide-dominated basins, including, among others, ichnology, clay mineralogy and/or the analysis of bedform dynamics.

This work highlights the necessity to consider the effects of changes in physiography related to relative sea-level variations and their associated impact on tidal dynamics, which will improve and refine models of tide-dominated basins. This increased knowledge of past basins will help to comprehend how tidal processes will evolve in response to ongoing sea-level rise and physiographic changes.

ACKNOWLEDGEMENTS

The authors of this paper thank the Norwegian Research Council for their awarded Personal Overseas Research Grant (ref. Number 295061), which allowed the main author to attend Queen's University in Kingston, Canada, as a visiting scholar for six months. The Norwegian Research Council is to be further acknowledged for its COTEC grant (ref. Number 295061). Dr Alexander Rey at Queen's University is recognized for help setting up the Delft3D model. JAMG acknowledges funding from the UK Natural Environment Research Council, grant NE/S009566/1 (MATCH). The authors thank Dr Hannah Louise Brooks for her fruitful comments on parts of the manuscripts and its figures, David Hadley-Pryce for his insight on initial tidal forcing, and Dr Miquel Poyatos-Moré and Dr Anna van Yperen for discussions of the impacts that changes of palaeophysiography can have on the sequence stratigraphy of tide-dominated basins. Dr Luc Girod is also sincerely thanked, because without him, the first author of this manuscript would probably still be trying to fix his Georaster package. The two reviewers Andrew La Croix and Martin Wells who worked on an earlier version of this manuscript are to be sincerely thanked for their constructive observations and remarks, as well as Poppe L. de Boer who commented on the preprint version of this manuscript. Finally, all of the co-authors would sincerely like to thank the Associate Editor Massimiliano Ghinassi for his work that really helped improving the quality of this manuscript. Open access funding enabled and organized by ProjektDEAL.

CONFLICT OF INTEREST

There are no conflicts of interest in the preparation or publication of this work.

DATA AVAILABILITY STATEMENT

All of the simulations results and other data presented in this paper (>500 Gb) can be saved on an external hard-drive and sent by postal mail.

REFERENCES

Ager, D.V. (1973) *The Nature of the Stratigraphic Record*. John Wiley, New York, 114 pp.

Allen, P.A. (1997) *Earth Surface Processes*. Blackwell Science, Oxford.

Anderson, O.J. and **Lucas, S.G.** (1994) Middle Jurassic stratigraphy, sedimentation and paleogeography in the southern Colorado Plateau and southern High Plains. In: *Mesozoic Systems of the Rocky Mountain Region, USA* (Eds Caputo, M.V., Peterson, J.A. and Franczyk, K.J.), *SEPM, Rocky Mountain Section*, 299–314.

Anderson, T.H. (2015) Jurassic (170–150 Ma) bathe tracks of a continental-scale fault, the Mexico–Alaska megashear, from the Gulf of Mexico to Alaska. In: *Late Jurassic Margin of Laurasia: A Record Of Faulting Accommodating Plate Rotation* (Eds Anderson, T.H., Didenko, A.N., Johnson, C.L., Khanchuk, A.I. and MacDonald, J.H.), *Geological Society of America, Special Paper*, **513**, 107–188.

Anthony, E.J. and **Dobroniak, C.** (2000) Erosion and recycling of aeolian dunes in a rapidly infilling macrotidal estuary: the Authie, Picardy, northern France. *Geol. Soc. London Spec. Public.*, **175**(1), 109–121.

Anthony, E.J., **Mrani-Alaoui, M.** and **Héquette, A.** (2010) Shoreface sand supply and mid-to late Holocene aeolian dune formation on the storm-dominated macrotidal coast of the southern North Sea. *Mar. Geol.*, **276**(1–4), 100–104.

Apecechea, M.I., **Verlaan, M.**, **Zijl, F.**, **Le Coz, C.** and **Kernkamp, H.** (2017) Effects of self-attraction and loading at a regional scale: a test case for the Northwest European Shelf. *Ocean Dyn.*, **67**(6), 729–749.

Arns, A., **Wahl, T.**, **Dangendorf, S.** and **Jensen, J.** (2015) The impact of sea level rise on storm surge water levels in the northern part of the German Bight. *Coast. Eng.*, **96**, 118–131.

Ashall, L.M., **Mulligan, R.P.**, **Van Proosdij, D.** and **Poirier, E.** (2016) Application and validation of a three-dimensional hydrodynamic model of a macrotidal salt marsh. *Coast. Eng.*, **114**, 35–46.

Azhikodan, G. and **Yokoyama, K.** (2018) Sediment transport and fluid mud layer formation in the macro-tidal Chikugo river estuary during a fortnightly tidal cycle. *Estuar. Coast. Shelf Sci.*, **202**, 232–245.

Baas, J.H., **Baker, M.L.**, **Malarkey, J.**, **Bass, S.J.**, **Manning, A.J.**, **Hope, J.A.**, **Peakall, J.**, **Lichtman, I.D.**, **Ye, L.**, **Davies, A.G.**, **Parsons, D.R.**, **Paterson, D.M.** and **Thorne, P.D.** (2019) Integrating field and laboratory approaches for ripple development in mixed sand–clay–EPS. *Sedimentology*, **66**(7), 2749–2768.

Bjerrum, C.J. and **Dorsey, R.J.** (1995) Tectonic controls on deposition of Middle Jurassic strata in a retroarc foreland basin, Utah-Idaho trough, western interior, United States. *Tectonics*, **14**(4), 962–978.

Blackledge, B.W., **Green, J.A.M.**, **Barnes, R.** and **Way, M.J.** (2020) Tides on other earths: Implications for exoplanet and Palaeo-tidal simulations. *Geophys. Res. Lett.*, **47**(12), e2019GL085746.

Blakey, R.C. (2014) Paleogeography and paleotectonics of the western interior seaway, Jurassic-Cretaceous of North America. *Search Disc.*, **30392**, 72.

Blanchard, S., **Fielding, C.R.**, **Frank, T.D.** and **Barrick, J.E.** (2016) Sequence stratigraphic framework for mixed aeolian, peritidal and marine environments: Insights from the Pennsylvanian subtropical record of Western Pangaea. *Sedimentology*, **63**(7), 1929–1970.

Bockelmann, F.D., **Puls, W.**, **Kleeberg, U.**, **Müller, D.** and **Emeis, K.C.** (2018) Mapping mud content and median grain-size of North Sea sediments–A geostatistical approach. *Mar. Geol.*, **397**, 60–71.

Boucot, A.J., **Xu, C.**, **Morley, R.J.** and **Scotese, C.R.** (2013) Phanerozoic paleoclimate: An atlas of lithologic indicators of climate. In: *Phanerozoic Paleoclimate: Concepts in Sedimentology and Paleontology* (Eds Nichols, G.J. and Ricketts, B.), **11**, pp. 1–18. SEPM, Tulsa. https://doi.org/10.2110/sepmcsp.11

Brenner, R.L. and **Peterson, J.A.** (1994) Jurassic sedimentary history of the northern portion of the Western Interior Seaway, USA. In: *Mesozoic Systems of the Rocky Mountain Region, USA* (Eds Caputo, M.V., Peterson, J.A. and Franczyk, K.J.), *SEPM, Rocky Mountain Section*, 233–272.

Brown, M.M., **Mulligan, R.P.** and **Miller, R.L.** (2014) Modeling the transport of freshwater and dissolved organic carbon in the Neuse River Estuary, NC, USA following Hurricane Irene (2011). *Estuar. Coast. Shelf Sci.*, **139**, 148–158.

Burgess, P.M. and **Prince, G.D.** (2015) Non-unique stratal geometries: implications for sequence stratigraphic interpretations. *Basin Res.*, **27**(3), 351–365.

Byrne, H.M., **Green, J.A.M.**, **Balbus, S.A.** and **Ahlberg, P.E.** (2020) A key environmental driver of osteichthyan evolution and the fish-tetrapod transition? *Proc. R Soc. A*, **476**(2242), 20200355.

Caputo, M.V. and **Pryor, W.A.** (1991) Middle Jurassic tide- and wave-influenced coastal facies and paleogeography, upper San Rafael Group, east-central Utah. In: *Geology of East-Central Utah* (Ed. Chidsey, T.C.), pp. 9–27. Utah Geological Association, Salt Lake City.

Carless, S.J., **Green, J.A.M.**, **Pelling, H.E.** and **Wilmes, S.B.** (2016) Effects of future sea-level rise on tidal processes on the Patagonian Shelf. *J. Mar. Syst.*, **163**, 113–124.

Carr-Crabaugh, M. and **Kocurek, G.** (1998) Continental sequence stratigraphy of a wet eolian system: a key to relative sea-level change. In: *Relative Role of Eustasy, Climate, and Tectonics in Continental Rocks* (Eds Stanley, K.W. and McCabe, P.J.), *SEPM, Special Publication*, **59**, 213–228.

Cartwright, D. (2001) On the origins of knowledge of the sea tides from antiquity to the Thirteenth Century. *Earth Sci. History*, **20**(2), 105–126.

Collins, D.S., **Avdis, A.**, **Allison, P.A.**, **Johnson, H.D.**, **Hill, J.** and **Piggott, M.D.** (2018) Controls on tidal sedimentation and preservation: Insights from numerical tidal modelling in the Late Oligocene-Miocene South China Sea, Southeast Asia. *Sedimentology*, **65**(7), 2468–2505.

Collins, D.S., **Avdis, A.**, **Wells, M.R.**, **Dean, C.D.**, **Mitchell, A.J.**, **Allison, P.A.**, **Johnson, H.D.**, **Hampson, G.J.**, **Hill, J.** and **Piggott, M.D.** (2021) Prediction of shoreline–shelf depositional process regime guided by palaeotidal modelling. *Earth Sci. Rev.*, **223**, 103827.

Collins, D.S., **Johnson, H.D.** and **Baldwin, C.T.** (2020) Architecture and preservation in the fluvial to marine transition zone of a mixed-process humid-tropical delta: Middle Miocene Lambir Formation, Baram Delta Province, north-west Borneo. *Sedimentology*, **67**(1), 1–46.

Cosma, M., **Finotello, A.**, **Ielpi, A.**, **Ventra, D.**, **Oms, O.**, **D'Alpaos, A.** and **Ghinassi, M.** (2020) Piracy-controlled geometry of tide-dominated point bars: Combined evidence from ancient sedimentary successions and modern channel networks. *Geomorphology*, **370**, 107402.

Costas, S. and **FitzGerald, D.** (2011) Sedimentary architecture of a spit-end (Salisbury Beach, Massachusetts): The imprints of sea-level rise and inlet dynamics. *Mar. Geol.*, **284**(1–4), 203–216.

Crabaugh, M. and **Kocurek, G.** (1993) Entrada Sandstone: an example of a wet aeolian system. In: *The Dynamics and Environmental Context of Aeolian Sedimentary Systems* (Ed. Pye, K.), *Geological Society of London, Special Publication*, **72**, 103–126.

Daher, H., **Arbic, B.K.**, **Williams, J.G.**, **Ansong, J.K.**, **Boggs, D.H.**, **Müller, M.**, **Huber, M.** (2021) Long-term Earth-Moon evolution with high-level orbit and ocean tide models. *J. Geophys. Res. Planets*, **126**, e2021JE006875.

Dalrymple, R.W., **Duncan, A.M.**, **Ichaso, A.A.** and **Choi, K.S.** (2012) Processes, morphodynamics, and facies of tide-dominated estuaries. In: *Principles of Tidal Sedimentology* (Eds Davis R.A. and Dalrymple, R.W.), pp. 187–229. Springer Science and Business Media, Dordrecht.

Danise, S. and **Holland, S.M.** (2017) Faunal response to sea-level and climate change in a short-lived seaway: Jurassic of the Western Interior, USA. *Palaeontology*, **60**(2), 213–232.

Danise, S. and **Holland, S.M.** (2018) A sequence stratigraphic framework for the Middle to Late Jurassic of the Sundance Seaway, Wyoming: implications for correlation, basin evolution, and climate change. *J. Geol.*, **126**(4), 371–405.

Danise, S., **Price, G.D.**, **Alberti, M.** and **Holland, S.M.** (2020) Isotopic evidence for partial geochemical decoupling between a Jurassic epicontinental sea and the open ocean. *Gondwana Res.*, **82**, 97–107.

Darwin, G.H. (1898) *The tides and kindred phenomena in the solar system: The substance of lectures delivered in 1897 at the Lowell institute, Boston, Massachusetts*. Houghton, Mifflin and company, Boston.

Davies, H.S., **Green, J.A.** and **Duarte, J.C.** (2020) Back to the future II: tidal evolution of four supercontinent scenarios. *Earth Syst. Dynam.*, **11**(1), 291–299.

Davies, N.S. and **Shillito, A.P.** (2018) Incomplete but intricately detailed: The inevitable preservation of true substrates in a time-deficient stratigraphic record. *Geology*, **46**(8), 679–682.

Davis Jr, R.A., **Dalrymple, R.W.** (Eds.). (2012) *Principles of Tidal Sedimentology*. Springer Science and Business Media, Dordrecht, 661 pp.

De Raaf, J.F.M. and **Boersma, J.R.** (2007) Tidal deposits and their sedimentary structures (seven examples from Western Europe). *Netherlands J. Geosci./Geologie En Mijnbouw*, **50**(3), 479–504.

Dean, C.D., **Collins, D.S.**, **van Cappelle, M.**, **Avdis, A.** and **Hampson, G.J.** (2019) Regional-scale paleobathymetry controlled location, but not magnitude, of tidal dynamics in the Late Cretaceous Western Interior Seaway, USA. *Geology*, **47**(11), 1083–1087.

Demko, T.M., **Currie, B.S.** and **Nicoll, K.A.** (2004) Regional paleoclimatic and stratigraphic implications of paleosols and fluvial/overbank architecture in the Morrison Formation (Upper Jurassic), Western Interior, USA. *Sed. Geol.*, **167**(3–4), 115–135.

Doelling, H.H., **Sprinkel, D.A.**, **Kowallis, B.J.** and **Kuehne, P.A.** (2013) Temple Cap and Carmel Formations in the Henry Mountains Basin, Wayne and Garfield Counties, Utah. In: *The San Rafael Swell and Henry Mountains Basin—Geologic Centerpiece of Utah* (Eds Morris, T.H. and Ressetar, R.), pp. 279–318. Utah Geological Association Publication, Utah.

Dossett, T.S. (2014) *The First $^{40}Ar/^{39}Ar$ Ages and Tephrochronologic Framework for theJurassic Entrada Sandstone in Central Utah*. MSc Thesis. Brigham Young University, Provo, UT.

Elias, E.P.L., **Gelfenbaum, G.** and **Van der Westhuysen, A.J.** (2012) Validation of a coupled wave-flow model in a high-energy setting: The mouth of the Columbia River. *J. Geophys. Res.*, **117**, C09011.

Eriksson, K.A. (1977) Tidal deposits from the Archaean Moodies Group, Barberton Mountain Land, South Africa. *Sediment. Geol.*, **18**(1–3), 257–281.

Fan, D. (2012) Open-coast tidal flats. In: *Principles of Tidal Sedimentology* (Eds Davis R.A. and Dalrymple, R.W.), pp. 187–229. Springer Science and Business Media, Dordrecht.

Fang, G., **Kwok, Y.K.**, **Yu, K.** and **Zhu, Y.** (1999) Numerical simulation of principal tidal constituents in the South China Sea, Gulf of Tonkin and Gulf of Thailand. *Cont. Shelf Res.*, **19**(7), 845–869.

Finotello, A., **D'Alpaos, A.**, **Bogoni, M.**, **Ghinassi, M.** and **Lanzoni, S.** (2020) Remotely-sensed planform morphologies reveal fluvial and tidal nature of meandering channels. *Sci. Rep.*, **10**(1), 1–13.

Fritzen, M.R., **Cagliari, J.**, **Candido, M.** and **Lavina, E.L.C.** (2019) Tidal bar cyclicity record in the Lower Permian: The Rio Bonito Formation, Paraná Basin, southern Brazil. *Sed. Geol.*, **381**, 76–83.

Gilluly, J. and **Reeside Jr, J.B.** (1928) Sedimentary rocks of the San Rafael Swell and some adjacent areas in eastern Utah. *U.S. Geol. Surv. Prof. Pap.*, **150-D**, 61–110.

Gordeev, R.G., **Kagan, B.A.** and **Polyakov, E.V.** (1977) The effects of loading and self-attraction on global ocean tides: the model and the results of a numerical experiment. *J. Phys. Oceanogr.*, **7**(2), 161–170.

Green, J.A.M., **Davies, H.S.**, **Duarte, J.C.**, **Creveling, J.C.** and **Scotese, C.** (2020) Weak tides during Cryogenian glaciations. *Nat. Commun.*, **11**, 6227.

Green, J.A.M., **Huber, M.**, **Waltham, D.**, **Buzan, J.** and **Wells, M.** (2017) Explicitly modelled deep-time tidal dissipation and its implication for Lunar history. *Earth Planet. Sci. Lett.*, **461**, 46–53.

Green, J.A.M., **Molloy, J.L.**, **Davies, H.S.** and **Duarte, J.C.** (2018) Is there a tectonically driven Supertidal cycle? *Geophys. Res. Lett.*, **45**(8), 3568–3576.

Green, J.A. and **Pugh, D.T.** (2020) Bardsey–an island in a strong tidal stream: underestimating coastal tides due to unresolved topography. *Ocean Sci.*, **16**(6), 1337–1345.

Greenberg, D.A., **Blanchard, W.**, **Smith, B.** and **Barrow, E.** (2012) Climate change, mean sea level and high tides in the Bay of Fundy. *Atmos. Ocean*, **50**(3), 261–276.

Gugliotta, M., **Flint, S.S.**, **Hodgson, D.M.** and **Veiga, G.D.** (2015) Stratigraphic record of river-dominated crevasse subdeltas with tidal influence (Lajas Formation, Argentina). *J. Sediment. Res.*, **85**(3), 265–284.

Gugliotta, M., **Saito, Y.**, **Nguyen, V.L.**, **Ta, T.K.O.**, **Nakashima, R.**, **Tamura, T.**, **Uehara, K.**, **Katsuki, K.** and **Yamamoto, S.** (2017) Process regime, salinity, morphological, and sedimentary trends along the fluvial to marine transition zone of the mixed-energy Mekong River delta, Vietnam. *Continent. Shelf Res.*, **147**, 7–26.

Gugliotta, M. and **Saito, Y.** (2019) Matching trends in channel width, sinuosity, and depth along the fluvial to marine transition zone of tide-dominated river deltas: The need for a revision of depositional and hydraulic models. *Earth Sci. Rev.*, **191**, 93–113.

Haigh, I.D., **Pickering, M.D.**, **Green, J.M.**, **Arbic, B.K.**, **Arns, A.**, **Dangendorf, S.**, **Hill, D.F.**, **Horsburgh, K.**, **Howard, T.**, **Idier, D.**, **Jay, D.A.**, **Jänicke, L.**, **Lee, S.B.**, **Müller, M.**, **Schindelegger, M.**, **Talke, S.A.**, **Wilmes, S.-B.** and **Woodworth, P.L.** (2020) The tides they are a-Changin': A comprehensive review of past and future nonastronomical changes in tides, their driving mechanisms, and future implications. *Rev. Geophys.*, **58**(1), e2018RG000636.

Hayden, A.M., **Wilmes, S.B.**, **Gomez, N.**, **Green, J.A.M.**, **Pan, L.**, **Han, H.** and **Golledge, N.R.** (2020) Multi-Century Impacts of Ice Sheet Retreat on Sea Level and Ocean Tides in Hudson Bay. *J. Geophys. Res. Oceans*, **125**(11), e2019JC015104.

Hess, K. (2003) Water level simulation in bays by spatial interpolation of tidal constituents, residual water levels, and datums. *Cont. Shelf Res.*, **23**(5), 395–414.

Hill, D.F., **Griffiths, S.D.**, **Peltier, W.R.**, **Horton, B.P.** and **Törnqvist, T.E.** (2011) High-resolution numerical modeling of tides in the western Atlantic, Gulf of Mexico, and Caribbean Sea during the Holocene. *J. Geophys. Res.*, **116**, C10014.

Hintze, L.F. and **Kowallis, B.J.** (2009) *Geologic history of Utah*. Brigham Young University Studies, Provo, Utah. 225 pp.

Holland, S.M. and **Wright, S.N.** (2020) The Unconformity That Isn't: A Sequence-Stratigraphic Reinterpretation of the J-5 Unconformity and the Redwater-Windy Hill–Morrison Transition in Wyoming, USA. *J. Geol.*, **128**(3), 247–274.

Hori, K., **Saito, Y.**, **Zhao, Q.** and **Wang, P.** (2002) Architecture and evolution of the tide-dominated Changjiang (Yangtze) River delta, China. *Sediment. Geol.*, **146**(3–4), 249–264.

Hu, K., **Ding, P.**, **Wang, Z.** and **Yang, S.** (2009) A 2D/3D hydrodynamic and sediment transport model for the Yangtze Estuary, China. *J. Marine Syst.*, **77**(1–2), 114–136.

Idier, D., **Paris, F.**, **Le Cozannet, G.**, **Boulahya, F.** and **Dumas, F.** (2017) Sea-level rise impacts on the tides of the European Shelf. *Cont. Shelf Res.*, **137**, 56–71.

Imlay, R.W. (1947) Marine jurassic of black hills area, South Dakota and Wyoming. *Am. Asso. Petrol. Geol. Bull.*, **31**(2), 227–273.

Imlay, R.W. (1952) Correlation of the Jurassic formations of North America, exclusive of Canada. *Geol. Soc. Am. Bull.*, **63**(9), 953–992.

Imlay, R.W. (1980) Jurassic Paleobiogeography of the Conterminous United States in its Continental Setting. *U.S. Geol. Surv. Prof. Paper*, **1062**, 134.

James, N.P. and **Dalrymple, R.W.** (Eds.). (2010) *Facies Models 4*. Geological Association of Canada, 575 pp.

Jensen, P.H., **Sprinkel, D.A.**, **Kowallis, B.J.** and **Brown, K.D.** (2016) *Geologic Map of the Donkey Flat Quadrangle, Uintah County, Utah*. Utah Geological Survey, Salt Lake City, UT.

Jerolmack, D.J. and **Sadler, P.** (2007) Transience and persistence in the depositional record of continental margins. *J. Geophys. Res., Series F*, **112**(F3), 1–14.

Jordan, O.D. and **Mountney, N.P.** (2010) Styles of interaction between aeolian, fluvial and shallow marine environments in the Pennsylvanian to Permian lower Cutler beds, south-east Utah, USA. *Sedimentology*, **57**(5), 1357–1385.

Jordan, O.D. and **Mountney, N.P.** (2012) Sequence stratigraphic evolution and cyclicity of an ancient coastal desert system: the Pennsylvanian-Permian Lower Cutler Beds, Paradox Basin, Utah, USA. *J. Sediment. Res.*, **82**(10), 755–780.

Kowallis, B.J., **Hunt, J.E.**, **Sprinkel, D.A.**, **May, S.B.**, **Bradfield, T.D.** and **Brown, K.D.** (2018) Geologic Map of the Lake Mountain Quadrangle, Uintah County, Utah. *Utah Geol. Surv.*, **801**, 537–3300.

Kreisa, R.D. and **Moila, R.J.** (1986) Sigmoidal tidal bundles and other tide-generated sedimentary structures of the Curtis Formation, Utah. *Geol. Soc. Am. Bull.*, **97**(4), 381–387.

Kresning, B., **Hashemi, M.R.**, **Neill, S.P.**, **Green, J.M.** and **Xue, H.** (2019) The impacts of tidal energy development and sea-level rise in the Gulf of Maine. *Energy*, **187**, 115942.

Kuzyk, Z.Z.A., **Goñi, M.A.**, **Stern, G.A.** and **Macdonald, R.W.** (2008) Sources, pathways and sinks of particulate organic matter in Hudson Bay: Evidence from lignin distributions. *Mar. Chem.*, **112**(3–4), 215–229.

Kvale, E.P. (2006) The origin of neap–spring tidal cycles. *Mar. Geol.*, **235**(1–4), 5–18.

Kvale, E.P. and **Archer, A.W.** (1991) Characteristics of two, Pennsylvanian age, semidiurnal tidal deposits in the Illinois Basin, USA. In: *Clastic Tidal Sedimentology* (Eds Smith, D.G., Reinson, G.E., Zaitlin, B.A. and Rahmani, R.A.), *Canadian Society Petroleum Geologists Memories*, **16**, 79–188.

Laugie, M., **Donnadieu, Y.**, **Ladant, J.-B.**, **Green, J.A.M.**, **Bopp, L.** and **Raisson, F.** (2020) Stripping back the Modern to reveal the Cretaceous climate and temperature gradients. *Clim. Past.*, **16**, 953–971.

Lentz, S., **Guza, R.**, **Elgar, S.**, **Feddersen, F.** and **Herbers, T.** (1999) Momentum balances on the North Carolina inner shelf. *J. Geophys. Res*, **104**, 18205–18226.

Longhitano, S.G., **Mellere, D.**, **Steel, R.J.** and **Ainsworth, R.B.** (2012) Tidal depositional systems in the rock record: a review and new insights. *Sed. Geol.*, **279**, 2–22.

Mallinson, D., **Culver, S.**, **Leorri, E.**, **Mitra, S.**, **Mulligan, R.** and **Riggs, S.** (2018) Pamlico sound and the outer banks Barrier Islands, North Carolina, USA. In: *Barrier Dynamics and Response to Changing Climate* (Eds Moore, L. and Murray, A.), pp. 91–120. Springer, Cham.

Mansfield, G.R. and **Roundy, P.V.** (1916) Revision of the Beckwith and Bear River Formations of southeastern Idaho. *U.S. Geol. Surv. Prof. Paper*, **98**, 75–84.

Midtkandal, I. and **Nystuen, J.P.** (2009) Depositional architecture of a low-gradient ramp shelf in an epicontinental sea: The lower Cretaceous of Svalbard. *Basin Res.*, **21**, 655–675. https://doi.org/10.1111/j.1365-2117.2009.00399.x

Mitchell, A.J., **Allison, P.A.**, **Gorman, G.J.**, **Piggott, M.D.** and **Pain, C.C.** (2011) Tidal circulation in an ancient epicontinental sea: the Early Jurassic Laurasian Seaway. *Geology*, **39**(3), 207–210.

Mountney, N.P. (2006) Periodic accumulation and destruction of aeolian erg sequences in the Permian Cedar Mesa Sandstone, White Canyon, southern Utah, USA. *Sedimentology*, **53**(4), 789–823.

Müller, R.D., **Cannon, J.**, **Qin, X.**, **Watson, R.J.**, **Gurnis, M.**, **Williams, S.**, **Pfaffelmoser, T.**, **Seton, N.**, **Russel, S.H.J.** and **Zahirovic, S.** (2018) GPlates: building a virtual Earth through deep time. *Geochem. Geophys. Geosyst.*, **19**(7), 2243–2261.

Mulligan, R.P., **Mallinson, D.J.**, **Clunies, G.J.**, **Rey, A.**, **Culver, S.J.**, **Zaremba, N.**, **Leorri, E.** and **Mitra, S.** (2019b) Estuarine responses to long-term changes in inlets, morphology and sea level rise. *J. Geophys. Res. Oceans*, **124**, 9235–9257.

Mulligan, R.P., **Perrie, W.** and **Solomon, S.** (2010) Dynamics of the Mackenzie River plume on the inner Beaufort shelf during an open water period in summer. *Estuar. Coast. Shelf Sci.*, **89**(3), 214–220.

Mulligan, R.P., **Smith, P.C.**, **Tao, J.** and **Hill, P.S.** (2019a) Wind-wave and tidally driven sediment resuspension in a macrotidal basin. *Estuaries Coasts*, **42**(3), 641–654.

Mulligan, R.P., **Walsh, J.P.** and **Wadman, H.M.** (2015) Storm surge and surface waves in a shallow lagoonal estuary during the crossing of a hurricane. *J. Waterway Port Coastal Ocean Eng.*, **141**(4), A5014001.

Paola, C., **Ganti, V.**, **Mohrig, D.**, **Runkel, A.C.** and **Straub, K.M.** (2018) Time not our time: Physical controls on the preservation and measurement of geologic time. *Annu. Rev. Earth Planet. Sci.*, **46**, 409–438.

Parker, B.B. (2007) *Tidal Analysis and Prediction*. NOAA Spec. Publ. NOSCO-OPS 3, Silver Spring, MD.

Patterson-Wittstrom, J. (1980) Stratigraphy of the Jurassic Stump Formation. *Stratigraphy of Wyoming: 31st Annual Field Conference Guidebook*, 91–100.

Pelling, H.E., **Green, J.A.M.** and **Ward, S.L.** (2013) Modelling tides and sea-level rise: To flood or not to flood. *Ocean Model.*, **63**, 21–29.

Peterson, F. (1994) Sand dunes, sabkhas, streams, and shallow seas: Jurassic paleography in the southern part of the Western Interior Basin. In: *Mesozoic Systems of the Rocky Mountain Region, USA* (Eds Caputo, M.V., Peterson, J.A. and Franczyk, K.J.), *SEPM, Rocky Mountain Section*, 233–272.

Phillips, S.P., **Howell, J.A.**, **Hartley, A.J.** and **Chmielewska, M.** (2020) Tidal estuarine deposits of the transgressive Naturita Formation (Dakota Sandstone): San Rafael Swell, Utah, USA. *J. Sediment. Res.*, **90**(8), 777–795.

Pipiringos, G.N. and **Imlay, R.W.** (Eds.) (1979) Lithology and subdivisions of the Jurassic Stump Formation in southeastern Idaho and adjoining areas. *Geol. Survey Prof. Paper*, **1035-C**, 1–25.

Pipiringos, G.N. and **O'Sullivan, R.B.** (1978). Principal unconformities in Triassic and Jurassic rocks, western interior United States: a preliminary survey. *U.S. Geol. Sur. Prof. Paper*, **1035-A**, 1–29.

Prinsenberg, S.J. (1986) The circulation pattern and current structure of Hudson Bay. In: *Canadian Inland Seas. Elsevier Oceanography Series 44* (Ed. Martini, I.P.), pp. 187-204. Elsevier Science, Amsterdam.

Prinsenberg, S.J. and **Freeman, N.G.** (1986) Tidal heights and currents in Hudson Bay and James Bay. In: *Canadian Inland Seas. Elsevier Oceanography Series 44* (Ed. Martini, I.P.), 205–216. Elsevier Science, Amsterdam.

Pugh, D. and **Woodworth, P.** (2014) *Sea-Level Science: Understanding Tides, Surges, Tsunamis and Mean Sea-Level Changes*. Cambridge University Press, Cambridge, 395 pp.

Räsänen, M.E., **Linna, A.M.**, **Santos, J.C.** and **Negri, F.R.** (1995) Late Miocene tidal deposits in the Amazonian foreland basin. *Science*, **269**(5222), 386–390.

Richter, K., **Riva, R.E.M.** and **Drange, H.** (2013) Impact of self-attraction and loading effects induced by shelf mass loading on projected regional sea level rise. *Geophys. Res. Lett.*, **40**(6), 1144–1148.

van Rijn, L.C. (1993) *Principles of Sediment Transport in Rivers, Estuaries and Coastal Seas*. Aqua publications, Amsterdam, 790 pp.

Rivers, J.M., **Dalrymple, R.W.**, **Yousif, R.**, **Al-Shaikh, I.**, **Butler, J.D.**, **Warren, C.**, **Skeat, S.B.** and **Bari, E.M.A.** (2020) Mixed siliciclastic-carbonate-evaporite sedimentation in an arid eolian landscape: The Khor Al Adaid tide-dominated coastal embayment. *Qatar. Sediment. Geol.*, **408**, 105730.

Rossi, V.M., **Kim, W.**, **Leva López, J.**, **Edmonds, D.**, **Geleynse, N.**, **Olariu, C.**, **Steel, R.J.**, **Hiatt, M.** and **Passalacqua, P.** (2016) Impact of tidal currents on delta-channel deepening, stratigraphic architecture, and sediment bypass beyond the shoreline. *Geology*, **44**(11), 927–930.

Sellwood, B.W. and **Valdes, P.J.** (2006) Mesozoic climates: General circulation models and the rock record. *Sed. Geol.*, **190**(1–4), 269–287.

Simon, B. and **Page, J.** (2017) *Tidal Constituents*. Tides, Water Level and Currents Committee, International Hydrographic Organization. https://iho.int/mtg_docs/com_wg/IHOTC/IHOTC_Misc/TWCWG_Constituent_list.pdf.

Sinha, B. and **Pingree, R.D.** (1997) The principal lunar semidiurnal tide and its harmonics: baseline solutions for M2 and M4 constituents on the North-West European Continental Shelf. *Cont. Shelf Res.*, **17**(11), 1321–1365.

Sleveland, A.R.N., **Midtkandal, I.**, **Galland, O.** and **Leanza, H.A.** (2020) Sedimentary architecture of storm-influenced tidal flat deposits of the upper Mulichinco Formation, Neuquén Basin, Argentina. *Front Earth Sci.*, **8**, 219.

Smith, D.G., **Bailey, R.J.**, **Burgess, P.M.** and **Fraser, A.J.** (2015) Strata and time: probing the gaps in our understanding. In: *Strata and Time: Probing the Gaps in Our Understanding* (Eds Smith, D.G., Bailey, R.J., Burgess, P.M. and Fraser, A.J.), *Geological Society, London, Special Publications*, **404**, 1–10.

Sprinkel, D.A., **Doelling, H.H.**, **Kowallis, B.J.**, **Waanders, G.** and **Kuehne, P.A.** (2011) Early results of a study of Middle Jurassic strata in the Sevier fold and thrust belt, Utah. In: *Sevier Thrust Belt: Northern and Central Utah and Adjacent Areas* (Eds Sprinkel, D.A., Yonkee, W.A. and Chidsey T.C.), *Utah Geological Association*, **40**, 151–172.

Sztanó, O. and **de Boer, P.L.** (1995) Basin dimensions and morphology as controls on amplification of tidal motions (the Early Miocene North Hungarian Bay). *Sedimentology*, **42**(4), 665–682.

Taylor, G.I. (1920) I. Tidal friction in the Irish Sea. *Philos. Trans. R. Soc. London Series A*, **220**(571–581), 1–33.

Thorman, C.H. (2011) The Elko orogeny–A major tectonic event in eastern Nevada–western Utah. Sevier thrust belt—northern and central Utah and adjacent areas. In: *Sevier Thrust Belt: Northern and Central Utah and Adjacent Areas* (Eds Sprinkel, D.A., Yonkee, W.A. and Chidsey T.C.), *Utah Geological Association, Publication*, **40**, 117–129.

Uhl, D., **Jasper, A.** and **Schweigert, G.** (2012) Charcoal in the Late Jurassic (Kimmeridgian) of Western and Central Europe—palaeoclimatic and palaeoenvironmental significance. *Palaeobiodiv. Palaeoenviron.*, **92**(3), 329–341.

Uhlir, D.M., **Akers, A.** and **Vondra, C.F.** (1988) Tidal inlet sequence, Sundance formation (upper Jurassic), north-central Wyoming. *Sedimentology*, **35**(5), 739–752.

Vieira, L.V. and **dos Santos Scherer, C.M.** (2017) Facies architecture and high resolution sequence stratigraphy of an aeolian, fluvial and shallow marine system in the Pennsylvanian Piauí Formation, Parnaíba Basin, Brazil. *J. S. Am. Earth Sci.*, **76**, 238–256.

Wang, Y., **Wang, Y.P.**, **Yu, Q.**, **Du, Z.**, **Wang, Z.B.** and **Gao, S.** (2019) Sand-mud tidal flat morphodynamics influenced by alongshore tidal currents. *J. Geophys. Res. Oceans*, **124**(6), 3818–3836.

Ward, S.L., **Green, J.A.M.** and **Pelling, H.E.** (2012) Tides, sea-level rise and tidal power extraction on the European shelf. *Ocean Dyn.*, **62**(8), 1153–1167.

Ward, S.L., **Neill, S.P.**, **Van Landeghem, K.J.** and **Scourse, J.D.** (2015) Classifying seabed sediment type using simulated tidal-induced bed shear stress. *Mar. Geol.*, **367**, 94–104.

Ward, S.L., **Scourse, J.D.**, **Yokoyama, Y.** and **Neill, S.P.** (2020) The challenges of constraining shelf sea tidal models using seabed sediment grain size as a proxy for tidal currents. *Cont. Shelf Res.*, **205**, 104165.

Webb, D.J. (2014) On the tides and resonances of Hudson Bay and Hudson Strait. *Ocean Sci.*, **10**(3), 411–426.

Wells, M.R., **Allison, P.A.**, **Hampson, G.J.**, **Piggott, M.D.** and **Pain, C.C.** (2005a) Modelling ancient tides: the Upper Carboniferous epi-continental seaway of Northwest Europe. *Sedimentology*, **52**(4), 715–735.

Wells, M.R., **Allison, P.A.**, **Piggott, M.D.**, **Pain, C.C.**, **Hampson, G.J.** and **De Oliveira, C.R.** (2005b) Large sea, small tides: the Late Carboniferous seaway of NW Europe. *J. Geol. Soc.*, **162**(3), 417–420.

Wells, M.R., **Allison, P.A.**, **Piggott, M.D.**, **Gorman, G.J.**, **Hampson, G.J.**, **Pain, C.C.** and **Fang, F.** (2007) (2007), Numerical modelling of tides in the Late Pennsylvanian Midcontinent Seaway of North America with implications for hydrography and sedimentation. *J. Sediment. Res.*, **77**, 843–865.

Wells, M.R., **Allison, P.A.**, **Hampson, G.J.**, **Piggott, M.D.**, **Pain, C.C.** and **Dodman, A.** (2008) Investigating tides in the Early Pennsylvanian Seaway of NW Eurasia using the Imperial College Ocean Model. In: *Dynamics of Epeiric Seas: Sedimentological, Paleontological and Geochemical Perspectives* (Eds Holmden, C. and Pratt, B.R.), *Geological Association of Canada, Special Publication*, **48**, 363–387.

Wells, M.R., **Allison, P.A.**, **Piggott, M.D.**, **Hampson, G.J.**, **Pain, C.C.** and **Gorman, G.J.** (2010) Tidal modeling of an ancient tide-dominated seaway, part 2: the Aptian Lower Greensand seaway of Northwest Europe. *J. Sediment. Res.*, **80**(5), 411–439.

Wilcox, W.T. and **Currie, B.** (2008) Sequence Stratigraphy of the Jurassic Curtis, Summerville, and Stump formations, Eastern Utah and Northwest Colorado. In: *Hydrocarbon Systems and Production in the Uinta Basin, Utah* (Eds Longman, M.W. and Morgan, C.D.), *Rocky Mountain Association of Geologists and Utah Geological Association, Publication*, **40**, 9–41.

Yalin, M.S. and **Karahan, E.** (1979) Inception of sediment transport. *J. Hydr. Div.*, **105**(11), 1433–1443.

van Yperen, A.E., **Holbrook, J.M.**, **Poyatos-Moré, M.** and **Midtkandal, I.** (2019) Coalesced delta-front sheet-like sandstone bodies from highly avulsive distributary channels: the low-accommodation Mesa Rica Sandstone (Dakota Group, New Mexico, USA). *J. Sediment. Res.*, **89**(7), 654–678.

van Yperen, A.E., **Poyatos-Moré, M.**, **Holbrook, J.M.** and **Midtkandal, I.** (2020) Internal mouth-bar variability and preservation of subordinate coastal processes in low-accommodation proximal deltaic settings (Cretaceous Dakota Group, New Mexico, USA). *Deposit. Rec.*, **6**(2), 431–458.

Zuchuat, V., **Midtkandal, I.**, **Poyatos-Moré, M.**, **Da Costa, S.**, **Brooks, H.L.**, **Halvorsen, K.**, **Cote, N.**, **Sundal, A.** and **Braathen, A.** (2019a) Composite and diachronous stratigraphic surfaces in low-gradient, transitional settings: The J-3 "unconformity" and the Curtis Formation, east-central Utah, USA. *J. Sediment. Res.*, **89**(11), 1075–1095.

Zuchuat, V., **Sleveland, A.**, **Sprinkel, D.**, **Rimkus, A.**, **Braathen, A.** and **Midtkandal, I.** (2018) New insights on the impact of tidal currents on a low-gradient, semi-enclosed, epicontinental basin—the Curtis Formation, east-central Utah, USA. *Geol. Intermoun. West*, **5**, 131–165.

Zuchuat, V., **Sleveland, A.R.**, **Pettigrew, R.P.**, **Dodd, T.J.**, **Clarke, S.M.**, **Rabbel, O.**, **Braathen, A.** and **Midtkandal, I.** (2019b) Overprinted allocyclic processes by tidal resonance in an epicontinental basin: The Upper Jurassic Curtis Formation, east-central Utah, USA. *Deposit. Rec.*, **5** (2), 272–305.

Manuscript received 18 December 2020; revision 18 January 2022; revision accepted 21 January 2022

Supporting Information

Additional information may be found in the online version of this article:

Appendix S1. Python Code.

Appendix B. 1 M2 tidal cycle for every depth scenario, and with both 0.5 m and 2.0 m initial, open ocean tidal forcing.

Appendix C. Impact of changing the drag coefficient on tidal amplitude, maximum flow speed, and bed shear stress.